Remote Sensing of Environment 287 (2023) 113493

Contents lists available at ScienceDirect

Remote Sensing of Environment

journal homepage: www.elsevier.com/locate/rse

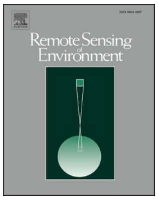

Improving the MODIS LAI compositing using prior time-series information

Jiabin Pu[a,b], Kai Yan[a,c,*], Si Gao[a], Yiman Zhang[a], Taejin Park[d], Xian Sun[e], Marie Weiss[f], Yuri Knyazikhin[b], Ranga B. Myneni[b]

[a] *School of Land Science and Techniques, China University of Geosciences, Beijing 100083, China*
[b] *Department of Earth and Environment, Boston University, Boston, MA 02215, USA*
[c] *Faculty of Geographical Science, Beijing Normal University, Beijing 100875, China*
[d] *Bay Area Environmental Research Institute, Ames Research Center, Moffett Field, CA 94035, USA*
[e] *Aerospace Information Research Institute, Chinese Academy of Sciences, Beijing 100094, China*
[f] *Institut National de la Recherche Agronomique—Université d'Avignon et des Pays du Vaucluse (INRA-UAPV), 228 Route de l'Aérodrome, 84914 Avignon, France*

ARTICLE INFO

Edited by Jing M. Chen

Keywords:
MODIS
VIIRS
Leaf area index (LAI)
Time-series compositing
Prior information
Time-series stability

ABSTRACT

The Moderate Resolution Imaging Spectroradiometer (MODIS) long-term leaf area index (LAI) products have significantly contributed to global energy fluxes, climate change, and biogeochemistry research. However, the maximum fraction of photosynthetically active radiation absorbed by vegetation (Max-FPAR) compositing strategy of the Collection 6 (C6) products dictates that the main or backup algorithm is always triggered by observations of different quality, which indirectly causes the observed instability in the LAI time-series. Based on MODIS daily LAI retrievals, this study develops a prior knowledge time-series compositing algorithm (PKA) using a linear kernel driven (LKD) model. Our results show that the newly proposed PKA can significantly improve the LAI composites compared to the Max-FPAR strategy using ground-based observations for validation. We found that the PKA performs better than Max-FPAR in various aspects (different sites, seasons, and retrieval index (RI) ranges), with R^2 increasing from 0.69 to 0.76 and root means square error (RMSE) decreasing from 1.01 to 0.84 compared to GBOV ground truth. The same improvement was shown for the ground truth LAIs measured at the Honghe and Hailun sites in northeastern China, with R^2 increasing from 0.23 to 0.41 and RMSE decreasing from 1.27 to 1.25. In addition, three newly proposed temporal uncertainty metrics (time-series stability, TSS and time-series anomaly, TSA and reconstruction error metric, RE (the proximity to the main RT-based retrievals)) were applied to compare the stability of LAI time-series before and after PKA implementation. We found that the time series stability of PKA LAI was improved, the time series anomalies were reduced, and the retrieval rates of the main algorithm were also greatly enhanced compared to Max-FPAR LAI. A case intercomparison for Max-FPAR-MODIS, Max-FPAR-VIIRS (Visible Infrared Imager Radiometer Suite), and PKA-MODIS LAIs in the Amazon Forest region showed that the PKA is also effective in improving the LAI retrieval over large regions with few qualified observations due to poor atmospheric conditions (RE decreased from 2.37/2.35 (Max-FPAR-MODIS/Max-FPAR-VIIRS) to 2.25 (PKA-MODIS) and RI increased from 61.94%/59.62% to 66.88%). The same improvement was seen in the BELMANIP 2.1 sites for almost all biomes except deciduous broadleaf forest, where the RE decreased from 1.85/2.13 to 1.15 overall. We note that the PKA has the potential to be easily implemented in the operational algorithms of subsequent MODIS and MODIS-like LAI Collections.

1. Introduction

The importance of terrestrial vegetation is widely recognized in various fields such as land-atmosphere interactions, biosphere, regulation of global carbon, water cycles, and energy cycles (Chen et al., 2022; Sellers et al., 1997). As an essential climate variable identified by the Global Climate Observing System (GCOS), leaf area index (LAI) is generally defined as half of the total green leaf area per unit of horizontal ground area, which is a fundamental parameter affecting the processes of radiation absorption, plant water balance, precipitation interception, and photosynthetic activity (Chen and Black, 1992; Fang et al., 2019a; Knyazikhin et al., 1998). Satellite remote sensing-derived global LAI products with decades-long series play an essential role in studies on the land surface carbon cycle, and global climate change,

---

[*] Corresponding author at: School of Land Science and Techniques, China University of Geosciences, Beijing 100083, China.
E-mail address: kaiyan.earthscience@gmail.com (K. Yan).

https://doi.org/10.1016/j.rse.2023.113493
Received 26 July 2022; Received in revised form 21 January 2023; Accepted 27 January 2023

among others (Asaadi et al., 2018; GCOS, 2011; Hill et al., 2006; Knyazikhin et al., 1998; Lafont et al., 2012; Sellers et al., 1997; Zhu et al., 2013). Therefore, the production of highly accurate long-term LAI datasets is essential for their appropriate use in land surface models and various user communities (Chen et al., 2022; Bi et al., 2015; Yin et al., 2017; Zhu et al., 2016).

The past few decades have witnessed an explosive growth in the number of satellites, resulting in >20 global-extent low or medium resolution long-term LAI datasets (e.g., Advanced Very High-Resolution Radiometer (AVHRR), Global Inventory Modeling and Mapping Studies (GIMMS), Moderate Resolution Imaging Spectroradiometer (MODIS), and Visible Infrared Imager Radiometer Suite (VIIRS)). The radiative transfer-based (RT-based) LAI products derived from surface reflectance have entered a new era since MODIS became operational in 2000 (Knyazikhin, 1999; Myneni and Park, 2015; Yan et al., 2016a). MODIS LAI products are commonly used as input and reference for the generation and intercomparison of other products (Baret et al., 2013; Park et al., 2017; Xiao et al., 2013; Yan et al., 2018; Yan et al., 2021c). Long-term MODIS LAI datasets have been widely applied to monitor the seasonal and interannual variability of temperate deciduous forests (Tang et al., 2013), investigate spatial trends in terminal drought (Chakroun et al., 2014; Dhorde and Patel, 2016; Mariano et al., 2018), and supporting various studies of global climate, biogeochemistry, and energy flux dynamics (Chen et al., 2022; Chen et al., 2019; Knyazikhin, 1999; Myneni and Park, 2015; Yan et al., 2016a; Zhang et al., 2017; Zhu et al., 2016). This product has contributed to several landmark studies, such as the "Greening Earth" phenomenon, possible reasons for large-scale vegetation dynamics, and the relationship between vegetation dynamics and global climate change or human activities (Chen et al., 2019; Chen and Dirmeyer, 2016; Mao et al., 2013; Zhang et al., 2017; Zhu et al., 2016).

However, as one of the most widely used LAI products, MODIS LAI still does not meet the uncertainty requirements proposed by GCOS (Fang et al., 2019a; Fang et al., 2019b). Furthermore, the relatively poor temporal continuity has been reported as one of the weaknesses of the MODIS LAI product, which limits its application for vegetation dynamic studies, especially in the tropics (Fang et al., 2012; Camacho et al., 2013). Previous studies have evaluated the uncertainty of MODIS LAI products through theoretical derivation (Fang et al., 2019a; Fang et al., 2013; Fang et al., 2012; Knyazikhin, 1999; Myneni et al., 2002; Park et al., 2017), intercomparison with other LAI products (Serbin et al., 2013; Yan et al., 2018; Yan et al., 2016a), and ground-based validation (Fang et al., 2012; Fuster et al., 2020; Liu et al., 2018; Weiss et al., 2014; Yan et al., 2016b). These studies indicated that the MODIS LAI uncertainty has two sources, i.e., the uncertainty in the inputs (land cover map and surface reflectance) and the uncertainty in the retrieval algorithm. Previous improvements to the MODIS LAI product have included two main aspects: 1) improvements to the forward RT models such as the stochastic radiative transfer (SRT) model coupled with more heterogeneity factors/hotspot effect (Li et al., 2020; Yan et al., 2021b); 2) revision to the retrieval algorithm such as the consideration of the proportion of water in the pixels (Xu et al., 2020). However, these improvements were focused on daily retrievals with good observations, which can do very little to reduce errors due to input uncertainties.

Surface reflectances are affected by clouds, aerosols, and poor sun-sensor geometry (Yan et al., 2021a; Weiss et al., 2007), and a temporal compositing process is always required to smooth the time-series by reducing the temporal resolution. The earliest temporal compositing methods used in remote sensing include maximum value compositing (MVC) (Holben, 1986), constrained maximum and minimum value composite (CM-MVC) (Cihlar et al., 1994), best index slope extraction from (BISE) (Viovy et al., 1992), mean compositing (MC) (Vancutsem et al., 2007), average compositing (AVG) (Ql and Kerr, 1997) and normalization of directional effect (Bacour et al., 2006), which focus on minimizing artifacts due to cloud or snow contamination, atmospheric or directional residual effects. And then, in order to smooth the time series of vegetation indices and to provide forecast over a season, some statistical methods including logistic curve fitting (Beck et al., 2006), asymmetric gaussian function curve fitting (Jönsson and Eklundh, 2004), savitsky-golay processing (Savitzky and Golay, 1964), and Fourier transform (Azzali and Menenti, 1999) have been proposed. For LAI products, the Global Land Surface Satellite (GLASS) LAI uses the general regression neural network (GRNN) for product generation (Xiao et al., 2013), and Verger et al. (2013) proposed a novel climatology fitting approach called consistent adjustment of the climatology to actual observations (CACAO) to reduce noise and fill gaps in LAI time series.

The MODIS LAI operational algorithm adopts the maximum fraction of photosynthetically active radiation absorbed by vegetation (Max-FPAR) compositing algorithm (detailed in Section 2.2) based on the assumption that poor observation conditions reduce the retrieved FPAR. However, the Max-FPAR compositing algorithm suffers from the following shortcomings: 1) it selects only one observation within an 8-day composite, and wastes the observation information of other days; 2) it likely selects the observation with the best atmospheric conditions but also potentially the poor sun-sensor geometry; 3) the intervals (1–15 days) between adjacent composites are not uniform, leading to greater uncertainty in phenology studies using the MODIS LAI product (Wang et al., 2017); 4) the inconsistent observation qualities contribute to the different algorithm paths of adjacent composites, which indirectly leads to fluctuations in the LAI time-series (Fang et al., 2019a; Fang et al., 2019b; Pu et al., 2020). These points limit the use of MODIS LAI products in forest ecosystem simulations (Li et al., 2019) and climate change models (e.g., North American Carbon Program (NACP)) that require high-quality temporal measurements (Huntzinger et al., 2013).

The current MODIS algorithm coupling the daily retrievals and the Max-FPAR compositing strategy that ignores the temporal correlation of reflectance, which could be used as prior knowledge to improve the smoothness of LAI time series. Recognizing the importance of using temporal correlation information, Geiger et al. (2008) improved the linear kernel driven (LKD) model by introducing temporal prior knowledge to better simulate the bidirectional reflectance factors (BRFs). This method has been used for directional effect normalization of AVHRR reflectance time series and to produce the Carbon Cycle and Change in Land Observational Products from an Ensemble of Satellites (CYCLOPES)/GLASS LAI products (Bacour et al., 2006; Baret et al., 2013; Xiao et al., 2013). A recent study used Geiger's method for correcting the directional effect of BRFs to improve the temporal continuity of normalized difference vegetation index (NDVI) (León-Tavares et al., 2021). Inspired by these studies, we realized the potential of implementing the time-series prior information into the LAI compositing process.

This research aims to develop a prior knowledge time-series compositing algorithm (PKA) for MODIS LAI products. The proposed PKA is expected to significantly improve the performance compared to the use of Max-FPAR and can be easily implemented into the current MODIS LAI production process. The structure of this paper is as follows. Section 2 describes the framework of the proposed PKA, including the data and evaluation indicators we used. Section 3 details the results of the comparison between PKA and Max-FPAR LAI compositing at both site and regional scales. We discuss the intrinsic causes of the improvements and prospects of PKA in Section 4. Finally, Section 5 provides concluding remarks.

2. Datasets and methods

2.1. Datasets and study area

2.1.1. MODIS daily surface reflectance: MOD09GA

The precursor to the MODIS LAI product is the MODIS daily surface reflectance with sun-sensor geometry and associated quality control (QC) flags, MOD09GA (Vermote et al., 2011; Vermote and Vermeulen,

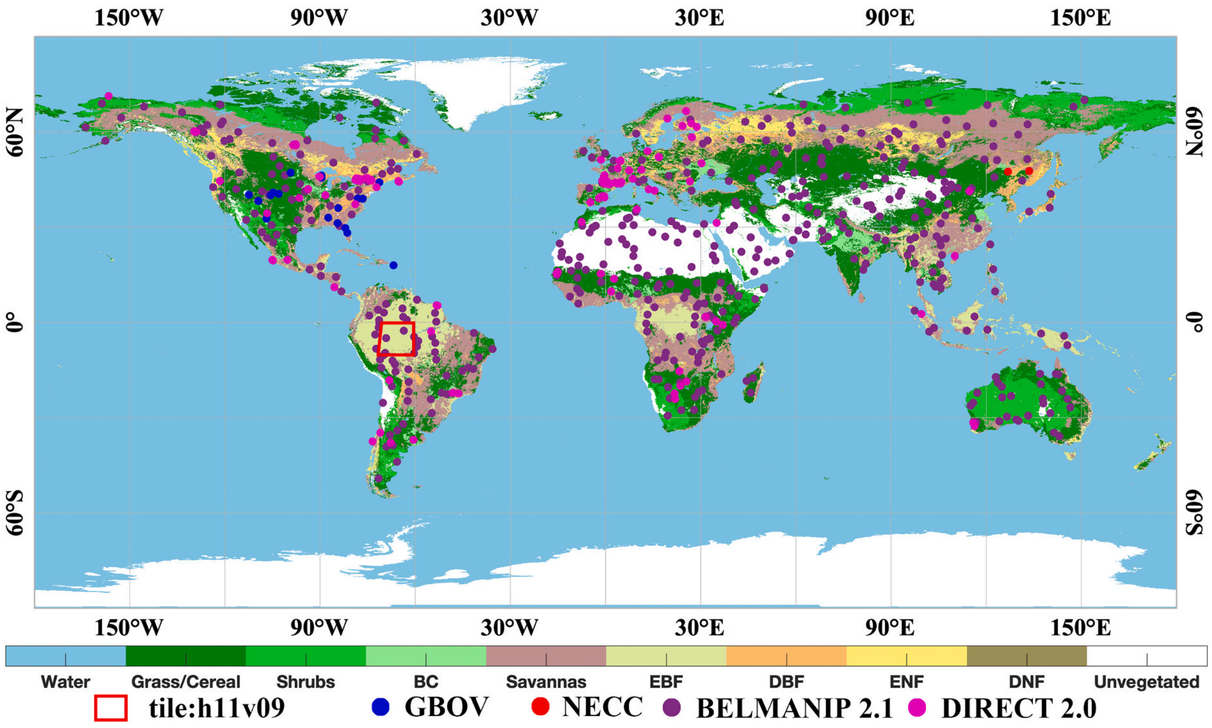

Fig. 1. Distribution of the selected GBOV/NECC/BELMANIP 2.1/DIRECT 2.0 sites and the specific study area in the Amazon Forests. The background colour indicates the biome types from the MCD12Q1 classification schemes of the year 2017. The blue/red/dark purple/bright purple dots represent the GBOV/NECC/BELMANIP 2.1/DIRECT 2.0 sites, and the red box is the selected tile h11v09. (For interpretation of the references to colour in this figure legend, the reader is referred to the web version of this article.)

1999). The current operational LAI algorithm inputs the BRFs in the red (strong vegetation absorption) and near-infrared (NIR) bands (strong vegetation scattering) to highlight the greenness/vegetation information and to estimate the LAI value. Although MOD09GA is a daily product, there may be multiple observations per day due to orbital overlaps, scanning bow-tie effects, and sampling strategies. Given that the number of samples varies with a MOD09GA product, the MODIS reflectance is compressed from two dimensions to one dimension in order to store additional observations with smaller storage space. Therefore, MOD09GA needs to be decompressed before it can be used to correctly correlate reflectance with sun-sensor geometry (Vermote et al., 2011). Then, we can obtain at least one set of observations per day (except for missing data due to instrumentation).

2.1.2. MODIS land cover map: MCD12Q1

The biome classification map is an auxiliary dataset for MODIS LAI and is used to reduce the uncertainties of the ill-posed retrieval process. Thus, an accurate biome classification map is essential to establish the correct connection between satellite observations and surface parameters. The MCD12Q1 is generated by classifying spectral-temporal features and maps the global biome types at 500-m spatial resolution and an annual time step (Sulla-Menashe and Friedl, 2018). In the MODIS LAI retrieval algorithm, one of the inputs is the MODIS land cover product (MCD12Q1) and different biome types have different configurations and preset parameters (Knyazikhin, 1999). The LAI algorithm uses the 8-vegetation-biome classification scheme (LC_Type_3) in MCD12Q1, i.e., B1: grasses and cereal crops; B2: shrubs; B3: broadleaf crops (BC); B4: savannas; B5: evergreen broadleaf forests (EBF); B6: deciduous broadleaf forests (DBF); B7: evergreen needleleaf forests (ENF); and B8: deciduous needleleaf forests (DNF) (Sulla-Menashe and Friedl, 2018; Yan et al., 2016a). The approximate distribution of global vegetation is shown in Fig. 1.

2.1.3. LAI products: MOD15A2H and VNP15A2H

The Collection 6 (C6) MODIS LAI/FPAR product (MOD15A2H), derived from data acquired by the Terra platform, has a global spatial resolution of 500 m and a temporal resolution of 8 days. The projection of this product is the sinusoidal grid, and the data are distributed in the standard hierarchical data format (HDF). There are six layers (FPAR, LAI, FparLai_QC, FparExtra_QC, FparStdDev, and LaiStdDev) included in the MODIS LAI/FPAR product. In this study, we used the LAI and FparLai_QC layers, which store the LAI retrieval and the algorithm path information, respectively (Knyazikhin, 1999; Myneni and Park, 2015; Yan et al., 2016a). Additionally, as the successor of the MODIS sensor (including the daily retrieval algorithm and the Max-FPAR compositing algorithm), the VIIRS was designed to extend this valuable long-term data record and the VNP15A2H has the same spatial and temporal resolution as the MOD15A2H. In this study, we also used the Collection 1 VIIRS (VNP15A2H) LAI product to make intercomparisons with MODIS Max-FPAR, PKA LAIs in the Amazon Forest region and BELMANIP 2.1 sites.

2.1.4. Ground LAI reference

With the increasing trend of application of earth observation products, the product uncertainty revealed by ground measurements based validation is increasing emphasized (Baret et al., 2006; Fang et al., 2012; Yang et al., 2006). To evaluate the performance of LAI retrievals using the PKA, we used Copernicus ground-based observations for validation (GBOV) LAIs, northeastern China crops (NECC) LAIs and DIRECT 2.0 LAIs as ground references (Brown et al., 2020; Brown et al., 2021; Fang, 2021).

The GBOV service aims to develop and distribute robust in situ datasets from a selection of monitoring sites for systematic and quantitative validation of global land products (Bai et al., 2019; Brown et al., 2020). The GBOV reference database was created following quality control of existing in situ measurements. It includes top of canopy reflectance, surface albedo, LAI, FPAR, fraction of covered ground, soil moisture at 5 cm depth, and land surface temperature. The GBOV data can be accessed in the open GBOV portal (https://gbov.acri.fr). In this study, we selected the GBOV LAI maps from 2014 to 2018 as references and selected twenty 3 km × 3 km squares centered on the location of the sites as our study areas (Fig. 1). Thus, each site contains 36 MODIS LAI pixels. In addition, to improve the credibility of the ground truth LAI, we filtered the ground LAI reference in these 20 sites using the criterion of "clear pixel" >95%. The number of available validation data was 869, leaving 14 sites with sufficient data to compare the stability of the time series.

NECC LAIs measured by LAI-2200 and DHP in Honghe (2012, 2013, and 2019) and Hailun (2016) in the Heilongjiang Province (northeastern China) were used in this study (Fig. 1). The first site (47°39′N, 133°31′E) is located in Honghe paddy rice farm (Fang et al., 2014), and the second site (47°24′–47°26′N, 126°47′–126°51′E) is located in the Hailun city, which planted with maize, soybean, and sorghum (Fang et al., 2018). Among them, the Honghe site and the Hailun site each selected five plots for field measurements (https://doi.org/10.1594/PANGAEA.939444). Continuous field measurements were made throughout the whole growing season, ranging from day of year (DOY) of 160 to 280. High-resolution LAI reference maps of these sites were also produced from cloud-free HJ-1 (30 m), Landsat 7 ETM+ (30 m), and Sentinel-2A MSI (20 m) imagery. And the reference LAI mean and standard deviation values within a 3 km * 3 km extent in each site were extracted and provided in this dataset. Thus, based on the 500-m spatial resolution of MODIS LAI, we selected 6*6 up-scaled pixels centered on these plots for the study. And, similar to GBOV, we filtered the ground LAI reference in these plots using the criterion of "the standard deviation value should not be greater than 50% of the LAI mean value".

In this study, we also selected the DIRECT 2.0 ground measurements as truth (Fig. 1), which includes 140 sites and 242 samples from 2000 to 2017 (Garrigues et al., 2008; Camacho et al., 2013). According to the CEOS-LPV guidelines, these sites are available and have been processed. Additionally, the DIRECT 2.0 filters forest sites with no understory and expands the time series to 2017 (https://calvalportal.ceos.org/web/olive/site-description). Same as GBOV and NECC sites, each site contains 36 MODIS LAI pixels, and we also filtered the ground LAI reference in these plots using the same criterion as NECC. However, due to the fact that the DIRECT 2.0 sites do not have continuity in observations, we do not use these data directly as validation, but a certain reference in the process of sensitivity analysis of some parameters.

2.1.5. *Amazon forest region*

Tropical forests play a critical role in the global carbon cycle. Changes in Amazon Forests' carbon stocks are an important source of anthropogenic greenhouse gas emissions. Understanding the long-term response of Amazon Forest to land use and climate is critical for balancing the global carbon budget and improving climate projections. The scientific community has struggled to analyze the available satellite data in the presence of significant cloud cover and high aerosol concentrations (Bullock et al., 2020; Hilker et al., 2015; Qin et al., 2021; Rappaport et al., 2018; Rodig et al., 2019). Optical sensors can obtain fewer high-quality observations over the Amazon Forest than in other regions, which poses a huge problem for LAI retrieval in this region. Therefore, the Amazon Forest region is the best study area to compare the performance of two LAI compositing methods (including two different MODIS composited LAIs and VIIRS LAI). In this study, we selected tile h11v09 from 2016 to 2020, centered on the Amazon Forests region, as a study area, which extends from 71° W to 60° W and from 10° S to 0° S (Fig. 1). In addition, we studied in the h11v09 tile with the pixels that did not change in the land cover from 2016 to 2020.

2.1.6. *BELMANIP 2.1 sites*

We compared the MODIS PKA LAI, MODIS Max-FPAR LAI, and VIIRS Max-FPAR LAI over 445 Benchmark Land Multisite Analysis and Intercomparison of Products (BELMANIP) version 2.1 sites for the year 2021 (Baret et al., 2006). The BELMANIP 2.1 sites, located in relatively homogeneous and flat areas, are designed to represent the global variability of land biome types based on the GLC2000 land cover map (Bartholome and Belward, 2005). By using the BELMANIP 2.1 sites, we can not only reduce the computational volume globally but also reduces the additional uncertainty caused by geometric registration bias and land cover misclassification. In this study, we selected the 6 × 6 pixels areas centered on the site locations as our study area for each site (see Fig. 1). The number of available pixels for each biome type ranged from 83 (B8, deciduous needleleaf forests) to 4368 (B1, grasses and cereal crops) pixels.

2.2. *MODIS LAI/FPAR operational retrieval algorithm*

The current daily MODIS LAI/FPAR algorithm calculates the relationships between LAI/FPAR and BRF by forward simulations of radiative transfer models (RTM) and uses these relationships to calculate the LAI that best matches the input BRFs. The algorithm derives LAI using red and NIR bands (band 1 and band 2), their uncertainties, sun-sensor geometry (SZA: solar zenith angle, SAA: solar azimuth angle, VZA: view zenith angle, VAA: view azimuth angle), and a biome map as inputs. To reduce the complexity of retrieval, the retrieval algorithm assumes that the soil reflectance, leaf single scattering albedo, and leaf inclination angle distribution are known and provides separate settings for eight biome types in their corresponding look-up tables (LUT). Note that different biome types use different RT models in the current version of the algorithm. Herbaceous biomes are modeled using 1D RT due to their good continuity and consideration of the computational efficiency. Savannas are modeled by a stationary Poisson germ-grain stochastic process (SRT model) (Huang et al., 2008; Yan et al., 2021b; Yang et al., 2017). Forest biomes are based on a 3D RTM (3D structures are represented by columns uniformly (deterministically) spaced columns on the ground). For these RTMs, the MODIS retrieval algorithm first separates the wavelength-independent vegetation structure parameters from the spectral parameters using the "spectral invariance theory", and only intermediate variables are stored in the LUT instead of multi-band reflectance, greatly reducing the content of the LUT. Secondly, the algorithm reads the LUT file and generates the BRF and FPAR as a function of the parameters including LAI, single scattering albedo (SSA), canopy absorbance, canopy transmittance, soil reflectance, sun-sensor geometry, and reflectance wavelength. Among these, the FPAR describes the canopy absorption between 400 nm and 700 nm. The algorithm then traverses different LAIs using the above parameters and the RTMs, and the corresponding BRFs and FPARs can be calculated. Again, the given atmospheric corrected BRFs (MOD09GA) are compared with the modeled BRFs, and the LAI/FPAR are considered as a set of candidate values if the uncertainty complies with the requirements (red: <5% and NIR: <20%). Finally, all the LAI/FPARs are selected and weighted to obtain the mean values and standard deviation as the retrieved LAI/FPAR and their corresponding uncertainties (Knyazikhin, 1999; Knyazikhin et al., 1998), respectively.

In the case of highly dense canopies, the reflectance is saturated and insensitive to changes in canopy properties. In the retrieval process, the range of the corresponding LAI/FPAR increases within the uncertainty range. It is shown that the standard deviation of the LAI/FPAR is extremely large, and the uncertainty in the saturation condition is artificially reduced. Therefore, LAI/FPAR values retrieved under saturated conditions are less reliable than those generated by unsaturated BRFs. When the main algorithm fails to localize a solution, the BRF is far from retrieval space (e.g., caused by snow cover) or the SZA/VZA is too large (winter of high latitude), the backup algorithm is used to retrieve values through an empirical relationship between NDVI and LAI/FPAR (Myneni et al., 2002; Yan et al., 2018). Such algorithm paths are flagged in the quality assessment (QA) layer (Knyazikhin, 1999), which consists of the main algorithm without saturation (QA = 0), the main algorithm with saturation (QA = 1), the backup algorithm due to sun–sensor

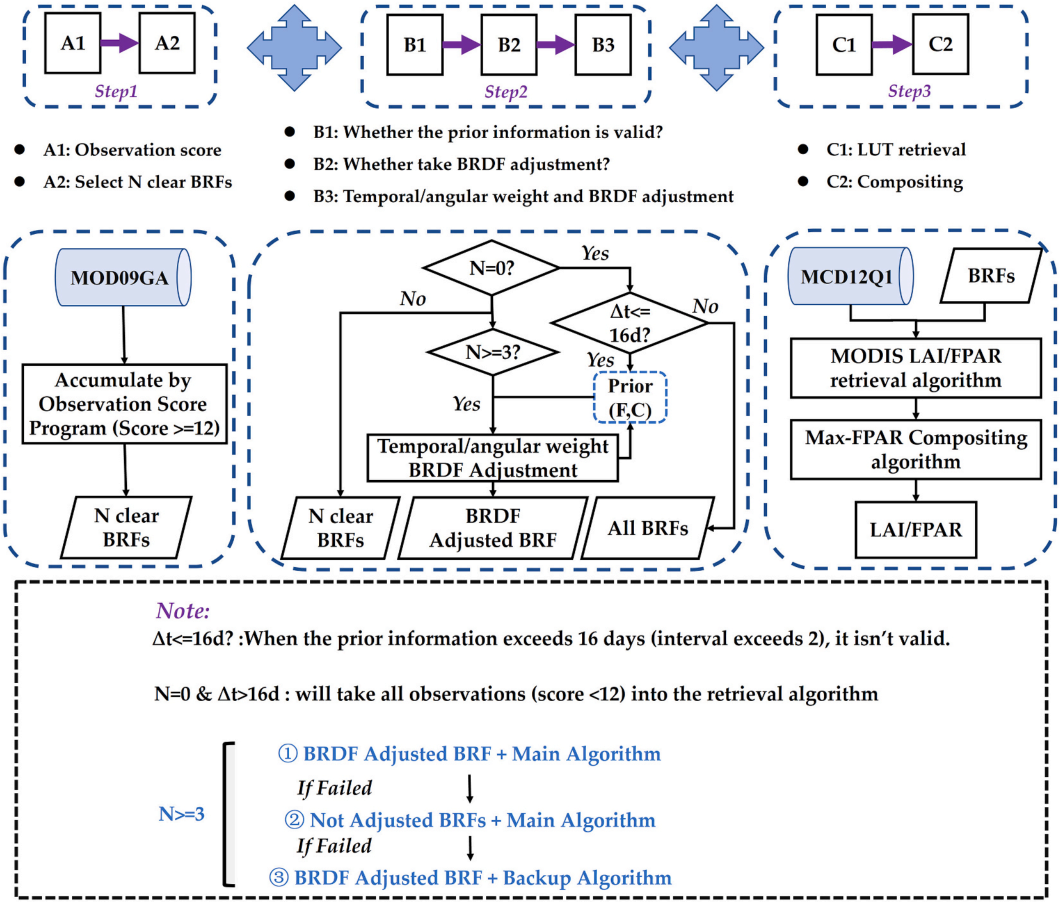

Note:

Δt<=16d? :When the prior information exceeds 16 days (interval exceeds 2), it isn't valid.

N=0 & Δt>16d : will take all observations (score <12) into the retrieval algorithm

N>=3

① BRDF Adjusted BRF + Main Algorithm
If Failed ↓
② Not Adjusted BRFs + Main Algorithm
If Failed ↓
③ BRDF Adjusted BRF + Backup Algorithm

Fig. 2. Framework of the MODIS LAI retrieval based on the proposed PKA strategy.

geometry (QA = 3), and the backup algorithm due to other reasons (QA = 4) (Yan et al., 2016a).

The daily retrieved LAI is very sensitive to the uncertainties in the daily inputs (caused by clouds, aerosols, and poor sun-sensor geometry) and is stored as an intermediate product that is not available to the public. To smooth the LAI time series, a temporal compositing process is applied by reducing the temporal resolution to 8-days. The MODIS compositing strategy can be divided into three components: 1) Select the best daily observation. The algorithm selects one best observation each day using an observation scoring procedure; 2) Main algorithm retrievals are preferred. If the main algorithm retrieval exists in the compositing period, all the main algorithm retrievals are selected as candidates; if there is no main algorithm retrieval exists, all the backup algorithm retrievals are selected as candidates; 3) Apply the Max-FPAR principle. Pick the date with the largest FPAR retrieval among all candidates in the compositing period, and the LAI value of that date is considered the optimal retrieval of this compositing period. The Max-FPAR compositing strategy is based on the fact that poor observation conditions reduce the retrieved FPAR (Holben, 1986).

2.3. *The proposed LAI temporal compositing algorithm*

Based on this semi-empirical BRDF model (RossThick-LiSparse-R BRDF model), León-Tavares et al. (2021) introduced an adaptive data accumulation window to reduce the NDVI time-series noise, and Roujean et al. (2018) performed a correction to surface directional effects that globally mapped surface albedo and normalized reflectance at 300 m. In addition, Chen et al. (2017) used a unique spatiotemporal imagery processing technique (i.e., the use of time series to improve accuracy and stability of the surface BRF) in the MODIS Multi-Angle Implementation of Atmospheric Correction (MAIAC) operational algorithm to improve the LAI retrieval accuracy, which indirectly highlights the value of using time series prior information in retrieval algorithms. We performed the BRDF correction of MODIS time-series reflectance to improve the LAI compositing using a similar method.

Inspired by these studies, a general prior knowledge time-series compositing algorithm was developed to improve the MODIS LAI retrieval accuracy and time series stability. This newly proposed algorithm combines the MODIS operational LAI algorithm and the bidirectional reflectance distribution function (BRDF) adjustment for the temporal compositing process, which is coupled with time series prior information. It mainly includes three parts: 1) performed screening of BRFs based on the official scoring program selected the high-quality BRFs; 2) temporal/angular weighting and BRDF adjustment; 3) retrieval/compositing algorithm. Notley, the PKA is not a simple fusion of the BRDF adjustment model with the MODIS LAI/FPAR retrieval algorithm. A detailed description of the processing stages is given in Fig. 2 and the following subsections.

2.3.1. *Framework of the refined MODIS operational LAI algorithm*

Considering the lack use of qualified observations in the current time window and temporal prior information, the PKA would fully utilize all qualified observations and time-series prior information based on angular/temporal weighting and BRDF adjustment (Fig. 2). And the steps are generally as follows.

In step 1, the PKA would first obtain the 'band data quality', 'perform atmospheric correction or not', 'cloud state', 'cloud shadow', and 'aerosol quantity' (representing the surface reflectance data quality) from the 'QC_500m' and 'state_1km' layers of MOD09GA. The data quality was then scored using the MODIS operational observation

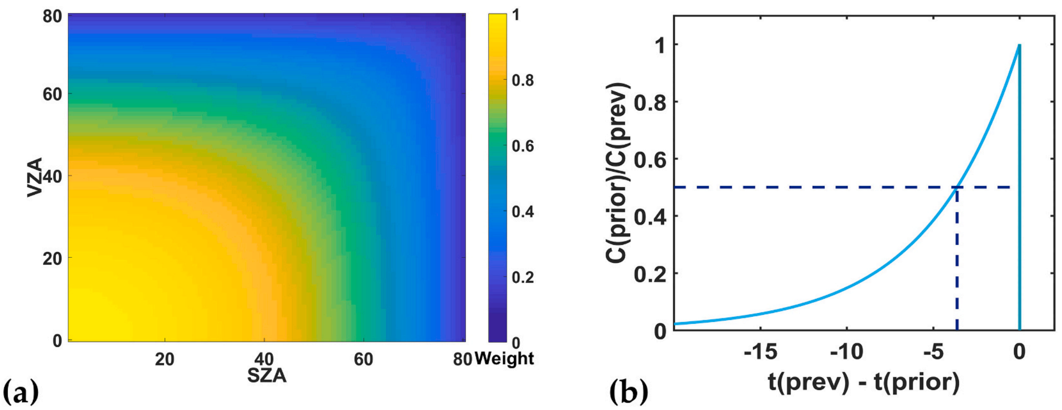

Fig. 3. Effectively angular weight (a) and temporal weight (b) functions in the recursive composition scheme.

scoring procedure (Table S1). All observations with a score >12 (N BRFs) in the time window (8 days) are selected, which means that all BRF pairs are corrected from the atmosphere and not flagged as cloud or cloud shadow. In contrast to the Max-FPAR algorithm,which selects the best observations each day, the PKA can take all high-quality observations as input, thus avoiding the waste of qualified observations.

Next in step 2, the time difference (Δt) between the current time window and the date of the prior information determines whether the prior information is plausible. Given the unreliability of the prior information in the case of large gaps, we set a threshold of 16 days for Δt. Then, it should then be noted that only one or two valid observations (least squares principle) are not required for the solution of the BRDF adjustment model (detailed in section 2.3.2). Therefore, the N and the Δt are used to determine whether to perform BRDF adjustment since that the retrieval confidence increases with the increased number of available BRFs and the proximity of prior information. The specific situation is as follows: 1) If $N \geq 3$, the BRDF adjustment is performed and the observation with the smallest SZA and VZA is selected as the specific angle to generate BRFs; 2) If $N = 1$ or 2, output the N clear BRFs (score ≥12); 3) If $N = 0$ and $\Delta t \leq 16$ days, take the BRDF inversion without BRDF adjustment, where the SZA is 0 and VZA = 0; 4) If N = 0 and $\Delta t >$ 16 days, the algorithm would use the all observations (including scores <12) in the current time window for output BRFs.

Finally in step 3, the algorithm would perform the LAI/FPAR retrieval and compositing process. In the case of N ≥3, if the retrieval algorithm path for BRDF-adjusted BRFs is main, output the retrieval LAI_B/FPAR_B directly; but if the algorithm path is backup, first record the current LAI_B/FPAR_B and input N clear BRFs to the retrieval algorithm. In this case, if there is more than one main algorithm-based retrieval, it will be composited by the Max-FPAR principle, but if all retrieval algorithms are all backup, LAI_B/FPAR_B will be used as output LAI/FPAR.

In summary, without changing the daily retrieval, when the number of qualified observations is sufficient, the PKA can use all the qualified observations, remove the directional effect of the observations, and provide time prior knowledge for the following retrievals; when there are fewer qualified observations, the PKA can make use of all available valid information and the time prior knowledge to perform the retrieval better. As shown in Fig. 2, the input and core retrieval algorithm of PKA is same as the original retrieval algorithm, which means that the PKA would easily replace the Max-FPAR based algorithm.

2.3.2. BRDF adjustment using time-series prior information

The magnitude of surface reflectance obtained for the same land surface is affected by the sun-sensor geometry and wavelength. The BRDF can be quantified by the inversion of an LKD model with three free parameters, which allows considering the reflectance anisotropy (Roujean, 2000; Roujean, 2018; Roujean et al., 1992; Wanner et al., 1995). When performing inversions, these three parameters are assumed not to change over a period. The initial equation of the RossThick-LiSparse-R BRDF model is as follows:

$$\rho(\theta_s,\theta_v,\varphi_r) = f_{iso}k_{iso} + f_{vol}k_{vol}(\theta_s,\theta_v,\varphi_r) + f_{geo}k_{geo}(\theta_s,\Theta_v,\varphi_r) = \sum_{i=iso,vol,geo} f_i k_i \quad (1)$$

where, θ_s is the SZA, θ_v is the VZA, φ_r is the sun-sensor relative azimuth angle (RAA), $\rho(\theta_s,\theta_v,\varphi_r)$ is the directional reflectance, k_{iso} is the isotropic scattering kernel and usually set to 1, k_{vol} is the volume scattering kernel, k_{geo} is the geometric optical kernel; f_{iso}, f_{vol} and f_{geo} represent the weights of isotropic scattering, volume scattering, and geometric optical scattering kernels, respectively.

Given a set of n ($n \geq 3$) observed surface reflectances under different sun-sensor geometries, this model can be inverted to get the BRDF. The above solution can be performed by finding the wavelength-dependent kernel weights (f_{iso}, f_{vol}, and f_{geo}). In addition, the reflectance of an arbitrary sun-sensor geometry can be estimated by the RossThick-LiSparse-R BRDF model used to describe the anisotropy of the surface reflectance. Eq. (1) is an equation system that can be rewritten as follows:

$$\mathrm{P} = KF \quad (2)$$

where, $K = [k_{ji}]$ is an (n × 3) matrix containing isotropic scattering, volume scattering, and geometric optical scattering kernels for the ensemble of n observations, F is a (3 × 1) vector $[f_{iso}, f_{vol}, f_{geo}]$, $\mathrm{P} = [\rho_j]$ is an (n × 1) vector of the observed reflectance ($j = 1,\ldots,n$) within a synthetic time window. BRDF inversion is well known as an ill-posed problem, where qualified observations may not exist over a period due to atmospheric conditions such as clouds and aerosols, or there are too many measurements which would introduce more uncertainties (Hagolle et al., 2005; Quaife and Lewis, 2010; Wang et al., 2007). However, the surface characteristics do not change in a brief period, which means that the BRDF model coefficients F also changes relatively little in a short period. Thus, Geiger et al. (2008) proposed a method that uses the prior information from previous BRDF inversion and ensures a smooth evolution of the F obtained from the previous inversion.

The BRDF adjust method first weight the P and K (the weight method is shown in Eq. (3)) within the time window.

$$w = 0.5(c_1 + c_2\rho)\left(\frac{1}{cos(1.058\theta_s) + cos(1.058\theta_v)}\right)\Bigg]^{-1} \quad (3)$$

where w has smaller weight values at larger SZA and VZA (Fig. 3a), which is shown in Eq. (3). The coefficients c_1 and c_2 in Eq. (3) are wavelength-dependent and are taken from Geiger et al. (2008), which are discussed in the section 4.2 (the algorithm need low c_1 and high c_2). The 1.058 means that $\frac{cos(90^\circ)}{cos(85^\circ)}$, and the 85° is the threshold for SZA and

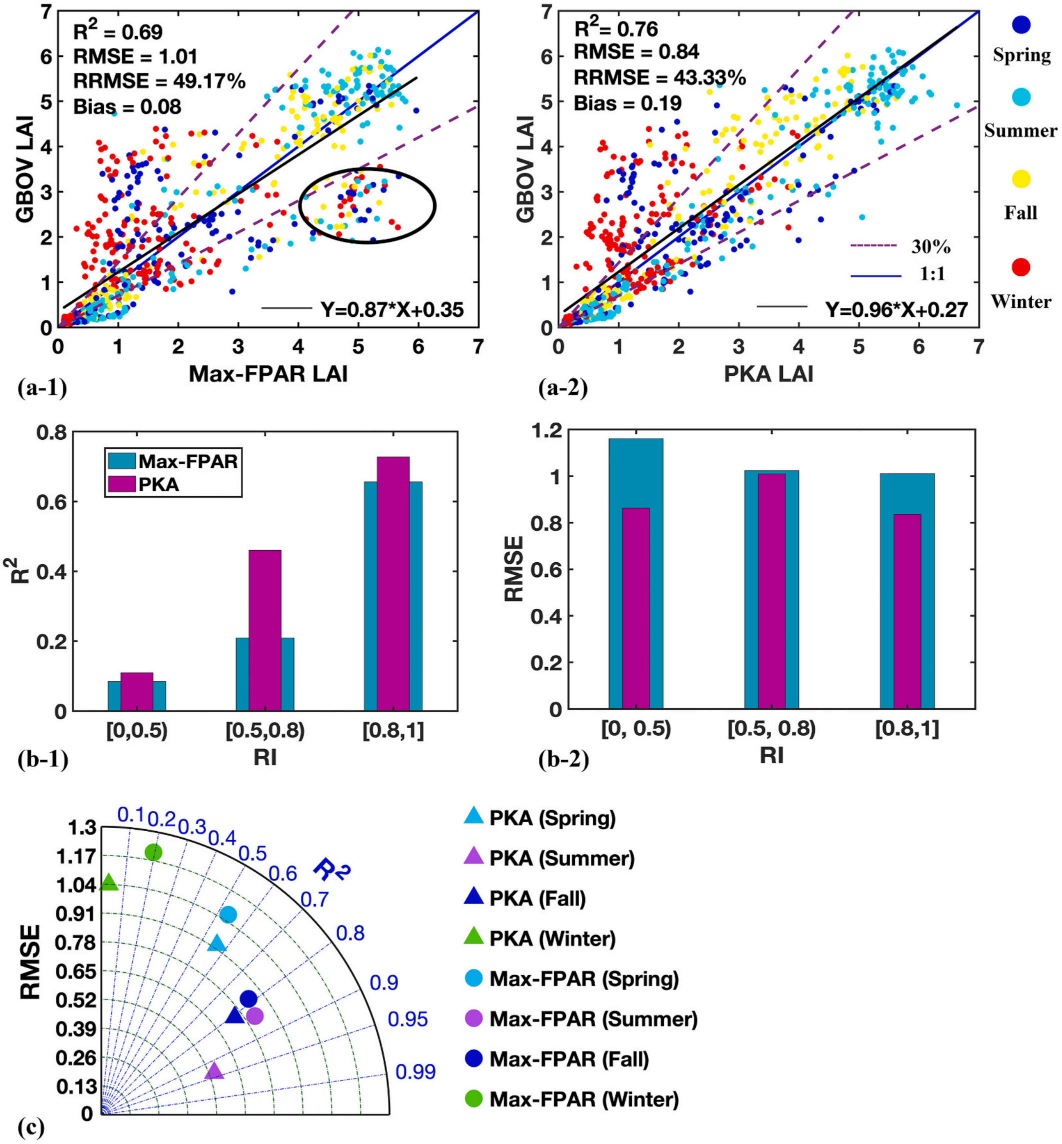

Fig. 4. (a) The scatter plot of the comparison between Max-FPAR LAI / PKA LAI and GBOV LAI measurements. (b) The R^2 and RMSE between Max-FPAR/PKA LAI and GBOV LAI in different RI ranges. (c) The R^2 and RMSE between Max-FPAR/PKA LAI and GBOV LAI measurement for different seasons.

VZA for the forward RTMs (Knyazikhin, 1999). Thus, the eq. (2) can be written as following eq. (4):

$$P^{w} = K^{w}F \tag{4}$$

This method then introduces temporal dimensional information by quantifying the correlation of the uncertainty of the prior information, which is shown in Eq. (5).

$$\left(K^{wT}K^{w} + C_{prior}^{-1}\right)F = K^{wT}P^{w} + C_{prior}^{-1}F_{prior} \tag{5}$$

where F_{prior} is a vector containing the values of F found in the previous BRDF inversion, C_{prior} (Eq. (6)) is a diagonal matrix, which contains the uncertainties of the prior information:

$$C_{prior} = C_{prev}(1+\Delta)^{(\Delta t)/\Delta_t} \tag{6}$$

$$(1+\Delta)^{(-\Delta)/8} = 0.5 \tag{7}$$

where Δ is the characteristic time scale, which means the full width at half mean of the weighing function (prior information until 16 days that weight <0.05, Fig. 3b).

From the above Eqs. (5)–(7), we can solve to obtain F (Eq. (8)) and C (Eq. (9)). In our proposed PKA, if $N = 0$ and $\Delta t > 16$, the C_{prior} and F_{prior} is unavailable, and if the $N = 0$ and $\Delta t \le 16$, the C and F means the C_{prior} and F_{prior}, respectively.

$$F = C\left(K^{wT}P^{w} + C_{prior}^{-1}F_{prior}\right) \tag{8}$$

$$C = \left(K^{wT}K^{w} + C_{prior}^{-1}\right)^{-1} \tag{9}$$

2.4. *Metrics for evaluating the PKA strategy*

In this paper, we quantify the fluctuation of a time-series using two recently proposed time-series metrics (Zou et al., 2022; Weiss et al., 2007) and one reconstruction error (RE) metric (Zhou et al., 2015; Zhou et al., 2016). These three metrics both indicate the temporal quality uncertainties of a dataset. Time-series stability (TSS) is defined as the distance from the value at the target moment t_0 to the linear interpolation line, which can be calculated from the data of the previous and the next time-series of the target moment date (Eq. (10)).

$$\mathrm{TSS}(t_0)=\frac{\left|(X(t_1)-X(t_{-1}))\times t_0-(t_1-t_{-1})\times X(t)-(X(t_1)-X(t_{-1}))\times t_{-1}+(t_1-t_{-1})\times X(t_{-1})\right|}{\sqrt{(X(t_1)-X(t_{-1}))^2+(t_1-t_{-1})^2}} \tag{10}$$

These two adjacent time-series data $X(t_1)$ and $X(t_{-1})$ were obtained at the moment t_{-1} (the previous data) and t_1 (the latter data), respectively. In this paper, we obtain the cumulative TSS, which means the higher TSS with the longer time-series theoretically. Therefore, the comparisons of TSS in this study are based on the same length of time-series.

We also used the standardized anomaly (SA) to quantify the anomaly of LAI time-series to better compare the fluctuation of different variables (Yan et al., 2018). SA was calculated as:

$$\mathrm{SA}(i)=\frac{\mathrm{T}(i)-\mathrm{mean}(\mathrm{prior}\ (\mathrm{i}))}{\mathrm{Std}(\mathrm{prior}\ (\mathrm{i}))} \tag{11}$$

where *T* and *i* are the variable time-series for one year and the time (DOY: 1:8:361), respectively. We first obtained the main RT-based LAI according to MOD15A2H and performed missing value filling to obtain prior LAI time-series for 20 years (2001–2020) *46 periods. Then, we used *T*(*i*) to indicate the Max-FPAR LAI and PKA LAI, the *prior* (*i*) means the prior LAI time-series (20*1) at different *i*. Finally, we used Eq. (11) to obtain *SA*(*i*). In this paper, we used the number of $|\mathrm{SA}| > 1$ to indicate the time-series anomaly. The time-series anomaly (TSA) is defined as the number of pixels greater than a threshold value:

$$\mathrm{TSA}=\mathrm{sum}(|\mathrm{SA}|\geq 1) \tag{12}$$

By comparing the retrieval time series with the reference series, the RE of each method can be quantified. As proposed by Zhou et al. (2015), the RE can be defined as the difference between the reference series and the retrieval series. In our study, we use the RE as one metric to quantify the closeness of the retrieval series and prior RT-based main retrieval series (Eq. (13)).

$$\mathrm{RE}=\sqrt[2]{\frac{\sum_{i=1}^{N}(\mathrm{retrieval}(i)-\mathrm{prior}(i))^2}{N}} \tag{13}$$

In addition, we used the RI (Eq. (14)), the percentage of pixels for which the RT-based main algorithm produces a retrieval (Xu et al., 2018; Yan et al., 2018; Yan et al., 2016b; Yan et al., 2021a), as one indicator of LAI retrieval uncertainty. The relative difference (RD, Eq. (15)) and absolute difference (AD, Eq. (16)) were also utilized to quantify the differences between retrieval and reference LAI.

$$\mathrm{RI}=\frac{\mathrm{N.of\ pixels\ retrieved\ by\ the\ main\ algorithm}}{\mathrm{N.of\ main\ algorithm}+\mathrm{N.of\ backup\ algorithm}} \tag{14}$$

$$\mathrm{RD}=(\mathrm{Retrieval}-\mathrm{Truth})/\mathrm{Truth} \tag{15}$$

$$\mathrm{AD}=|\mathrm{Retrieval}-\mathrm{Truth}| \tag{16}$$

3. Results

3.1. Validation using ground LAI measurements

Fig. 4 illustrates the results verified by ground-based measurements, where the PKA performed relatively better versus the MODIS Max-FPAR LAI. From Max-FPAR to PKA LAI, the R^2 increased from 0.69 to 0.76, the RMSE decreased from 1.01 to 0.84, and the RRMSE decreased from 49.17% to 43.33% (Fig. 4a), which can be attributed to the fact that the number of PKA LAI retrievals with bias exceeding 30% is less than Max-FPAR. Remarkably, the significant underestimation that was originally seen in the Max-FPAR LAI (circled in Fig. 4a-1) was removed in the PKA case (Fig. 4a-2), which also can explain why the bias increase from 0.08 to 0.19. However, the significant overestimation of the LAI retrievals in the winter season (red scatter dots with bias >30%) does not disappear

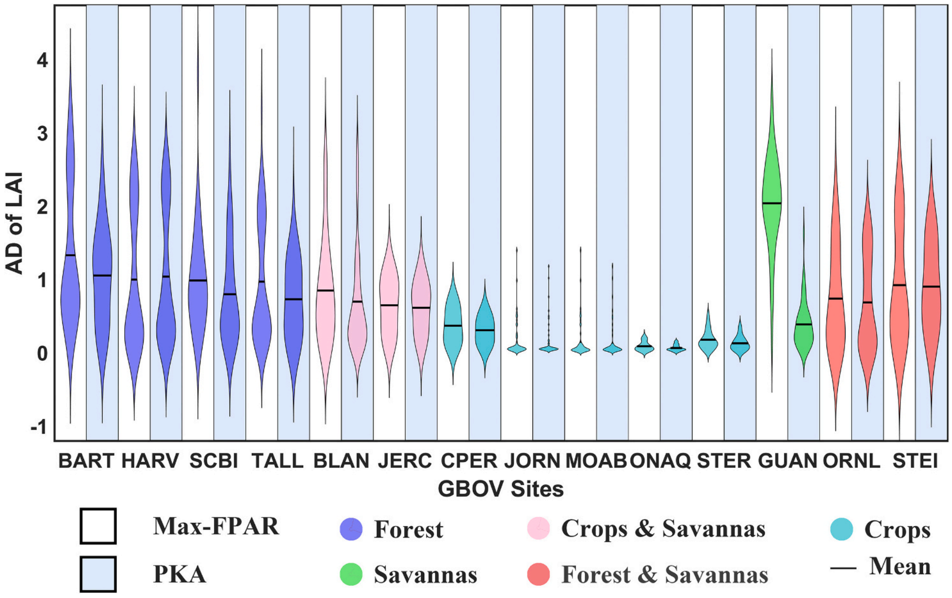

Fig. 5. The approximate range of AD of the LAI of five biome types for 14 GBOV sites. The white and blue backgrounds correspond to the Max-FPAR and PKA, respectively. The five biome types are forest, crops, savannas, crops & savannas, and forest & savannas. (For interpretation of the references to colour in this figure legend, the reader is referred to the web version of this article.)

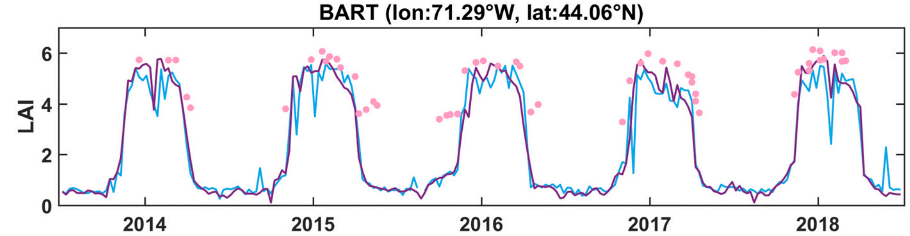

(a) Forest

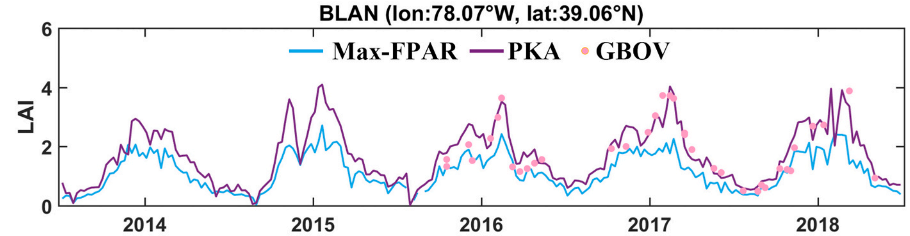

(b) Crops & Savannas

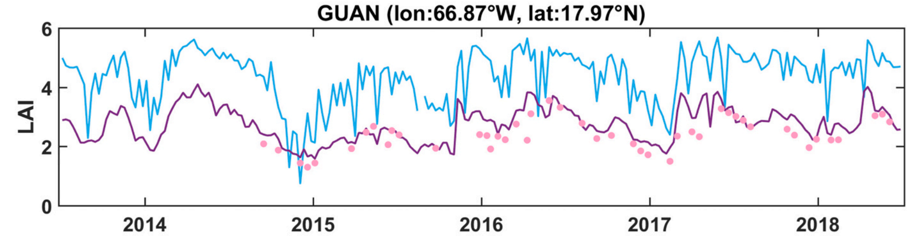

(c) Savannas

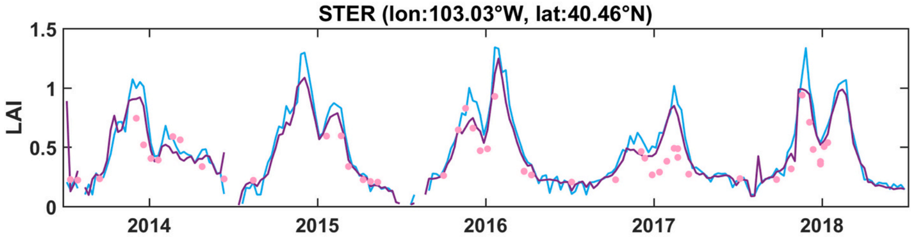

(d) Crops

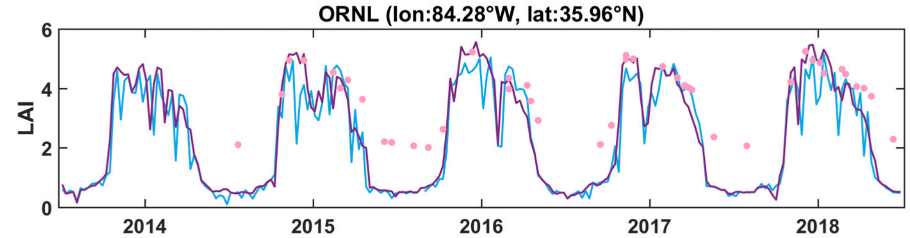

(e) Forest & Savannas

Fig. 6. LAI time-series comparison at five GBOV sites over the period from 2014 to 2018; the five sites represent different biome types. The Max-FPAR LAI derived from the MODIS C6 product and the newly proposed PKA LAI are shown as blue and purple lines, respectively. The pink dots are the GBOV ground-based LAI. (For interpretation of the references to colour in this figure legend, the reader is referred to the web version of this article.)

after PKA implementation (discussed in section 4). For both Max-FPAR and PKA, the R^2 were lower in winter than the other three seasons, opposite for RMSE (Fig. 4c). Thus, the retrieval accuracy also showed a clear seasonality (high accuracy in summer and low in winter) for both Max-FPAR and PKA LAI. We also noticed a significant improvement of the PKA in the different RI ranges, where the R^2 increased by about 0.02–0.21 and the RMSE are decreased by about 0.02–0.30 (Fig. 4b). This indicated that the PKA had a clear improvement on LAI retrievals using the backup algorithm. Similar conclusions can be drawn from the comparisons of different seasons (Fig. 4c), i.e., the R^2 was higher and the RMSE was lower for PKA except winter.

Additionally, for the 14 sites that still had sufficient validation data still existed after filtering, Fig. 5 shows that both the mean value and standard deviation of the AD of LAI showed a decreasing trend. For all selected GBOV sites, 13 of the 14 sites (except site HARV) showed a decreasing trend in the mean value of AD of LAI, while all sites showed a decreasing trend in the standard deviation of AD of LAI, demonstrating the improvement of PKA over Max-FPAR. For different biome types,

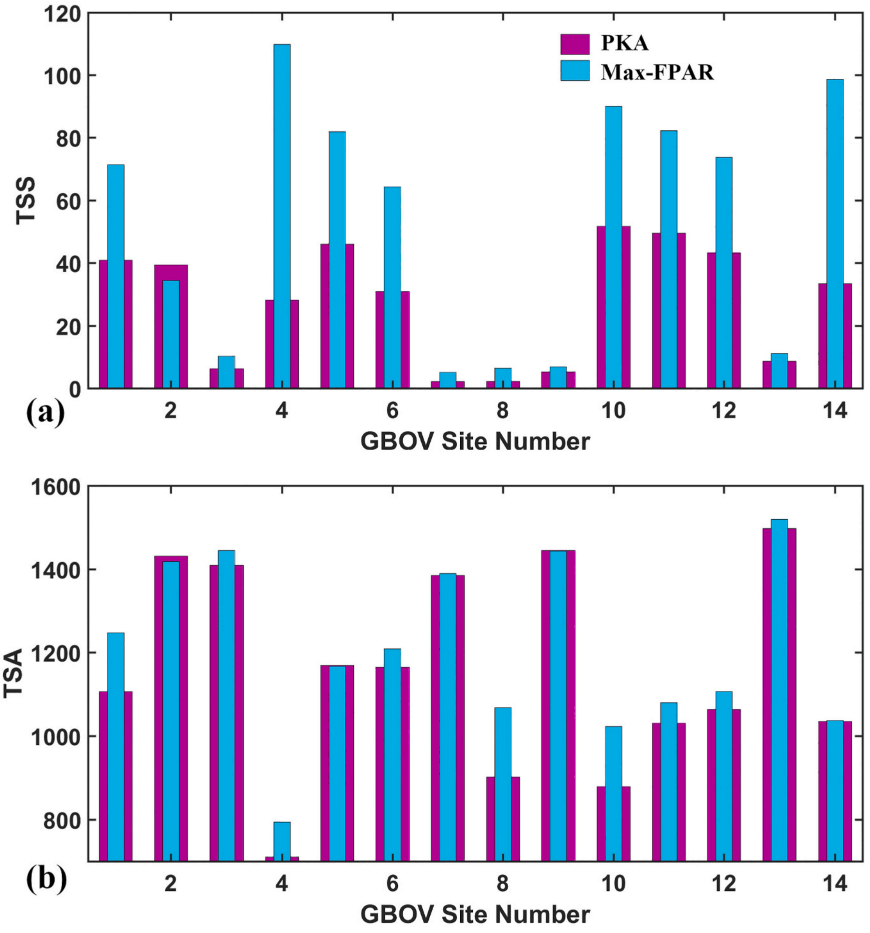

Fig. 7. Comparison of TSS (a) and TSA (b) for 14 GBOV sites between MODIS Max-FPAR LAI (blue) and PKA LAI (purple) from 2014 to 2018. The 14 sites are BART, BLAN, CPER, GUAN, HARV, JERC, JORN, MOAB, ONAQ, ORNL, SCBI, STEI, STER, and TALL. (For interpretation of the references to colour in this figure legend, the reader is referred to the web version of this article.)

Table 1
The coefficients c_1 and c_2 in Eq. (3).

	c_1	c_2
Red	0.001	0.07
NIR	0.005	0.02

savannas (GUAN site) showed a significant improvement; crops did not show a large trend decrease in the mean value of AD of LAI due to small LAI values, but the distribution of AD of LAI was more consistent; all other biome types indicated a slight decrease in the mean value and standard deviation of the AD of LAI.

3.2. Time-series comparison at site scale

The main purpose of this study was to improve the temporal stability of the retrieved LAI. We checked the degree of LAI temporal stability from both methods using two metrics (TSS and TSA) for the 14 GBOV sites (where TSS is the mean value of cumulative TSS of 36 pixels at each site over 5 years, and TSA is the sum of the number of pixels with abnormal SA for 36 pixels over 5 years) that provide a sufficient number of ground measurements (Fig. 6, Fig. S1, Fig. S2). The results showed that the PKA LAI had fewer fluctuations (did not follow the expected seasonal behavior, e.g., fluctuations of large magnitude in the time series) than Max-FPAR LAI (Fig. 6, Fig. S1, Fig. S2). In addition, underestimations of both Max-FPAR and PKA LAIs were clearly present in the winter seasons (Fig. 6a, e).

Table 2
Comparison of TSS, and TSA for Max-FPAR LAI, and PKA LAI for NECC sites (2012, 2013, and 2019 for Honghe and 2016 for Hailun).

Site		Honghe-2012	Honghe-2013	Hailun-2016	Honghe-2019	Overall
TSS	Max-FPAR	6.30	6.60	6.62	8.82	7.08
	PKA	4.06	7.11	4.78	5.60	5.39
TSA	Max-FPAR	1135	768	1135	1413	1113
	PKA	888	678	727	1590	971

As shown in Fig. 7a, the TSS of the LAI retrieved by the PKA was lower than that of Max-FPAR. The TSS showed a decreasing trend at 13 out of the 14 sites (except at site 2), while the mean value of the TSS of 14 sites decreased from 53.32 for Max-FPAR to 27.69 for PKA. This phenomenon indicated that the PKA substantially improved the stability of the time series compared to the currently used MODIS Max-FPAR LAI. The same situation was observed for TSA (Fig. 7b), where 11 sites presented a higher TSA for Max-FPAR than for the PKA (except for sites 2, 5, and 9). Overall, the PKA reduced the frequency of time-series anomalies.

Based on the ground observations of NECC LAIs provided by Fang et al. (2021), we also performed the associated time-series stability analysis using TSS and TSA (where, the TSS is the mean value of the 180 pixels for each of the 5 plots (6*6 pixels) combined for each year, while the TSA is the sum value of 180 pixels). The Fig. S3 and Table 2 indicated that the PKA LAI is more stable in the time-series than the Max-FPAR,

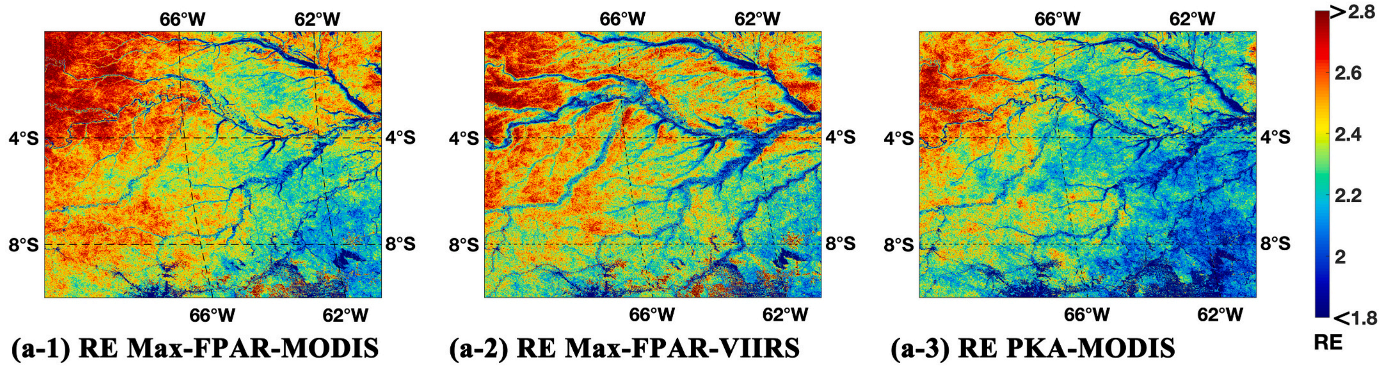

(a-1) RE Max-FPAR-MODIS (a-2) RE Max-FPAR-VIIRS (a-3) RE PKA-MODIS

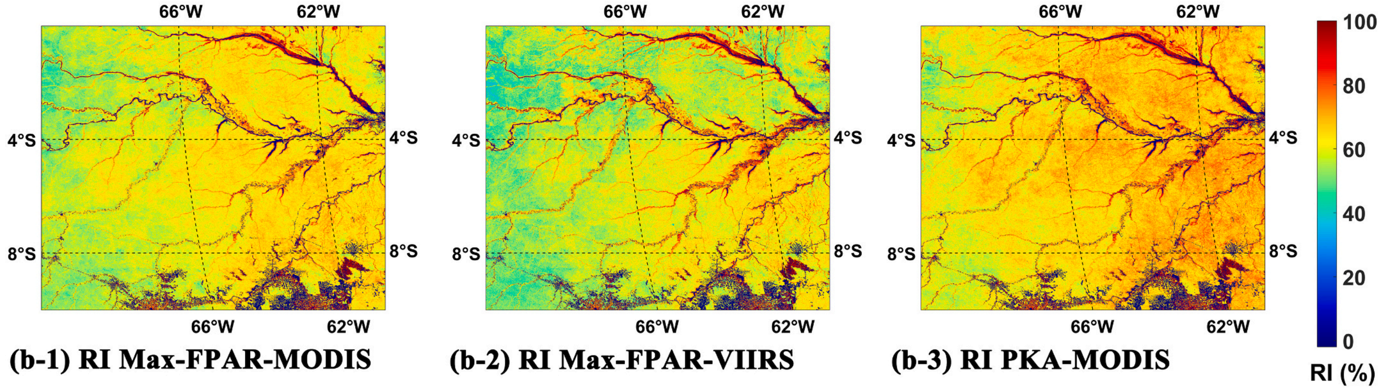

(b-1) RI Max-FPAR-MODIS (b-2) RI Max-FPAR-VIIRS (b-3) RI PKA-MODIS

Fig. 8. The spatial distribution of RE (a), and RI (b) in the tile h11v09 (Amazon Forest region) from 2016 to 2020. The 3 panels are Max-FPAR-MODIS LAI, Max-FPAR-VIIRS LAI, and PKA-MODIS LAI, respectively.

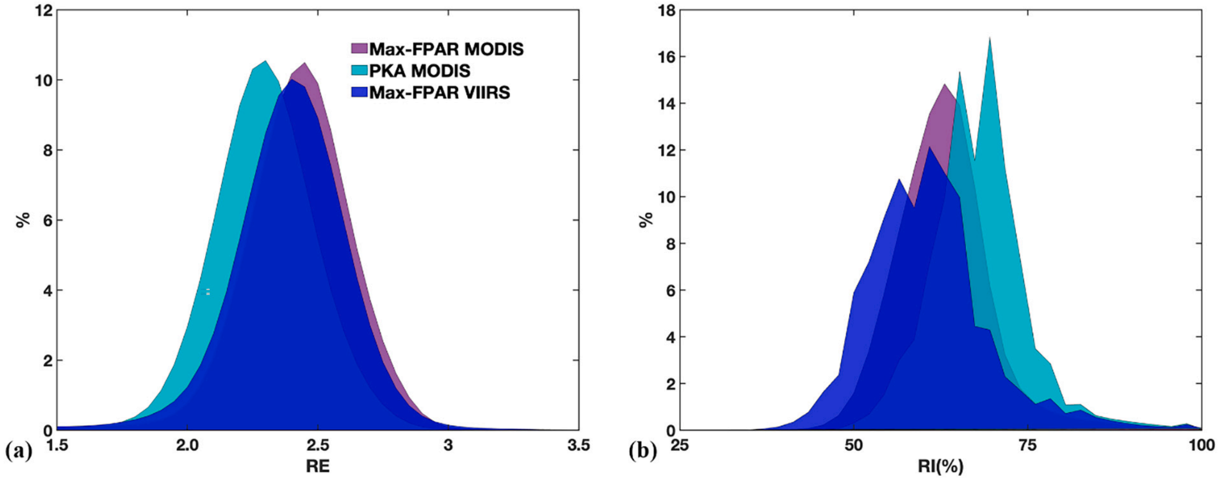

Fig. 9. Probability distribution of RE (a) and RI (b) in tile h11v09 from 2016 to 2020.

the TSS (except 2013 of Honghe) and the TSA (except 2019 of Honghe) all show the decreasing trend for four years. Combining four years' retrievals, from Max-FPAR to PKA, the TSS decreases from 7.08 to 5.39 and the TSA decreases from 1113 to 971 overall. In addition, the more significant phenomena include the fact that the PKA is closer to the ground reference LAIs than Max-FPAR in the early vegetation growth season (small DOY), which is mainly due to that PKA can eliminate the directional effect with sufficient observations. Whereas in the late vegetation growth season (large DOY), the SZA is large due to the higher latitude, leading to systematic overestimation for both PKA and Max-FPAR. Overall, compared to the ground truth LAI, the R^2 increased from 0.23 (Max-FPAR) to 0.41 (PKA) and the RMSE decreased from 1.27 to 1.25 (Fig. S4). Significantly, the underestimation of Max-FPAR was disappeared after the PKA implementation, PKA is closer to ground reference LAI than Max-FPAR.

3.3. Intercomparison over the Amazon Forest

Fig. 8 shows that the PKA-MODIS improved the performance more significantly than Max-FPAR-MODIS and Max-FPAR-VIIRS LAIs, while the Max-FPAR-MODIS and Max-FPAR-VIIRS LAIs are closer. Statically, the main biome type of the studied tile was EBF, the multi-year value of RE decreased from 2.40/2.37 (Max-FPAR-MODIS/Max-FPAR-VIIRS) to 2.27 (PKA-MODIS) and the proportion of the PKA using the main algorithm increased, and the RI increased from 61.99%/59.35% to 66.60%. When averaged over all biome types, the RE and RI all showed

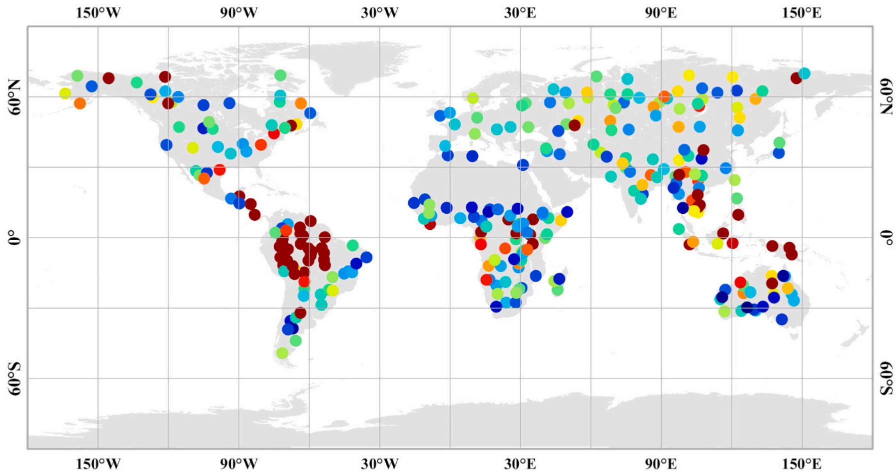

(a) Max-FPAR-MODIS

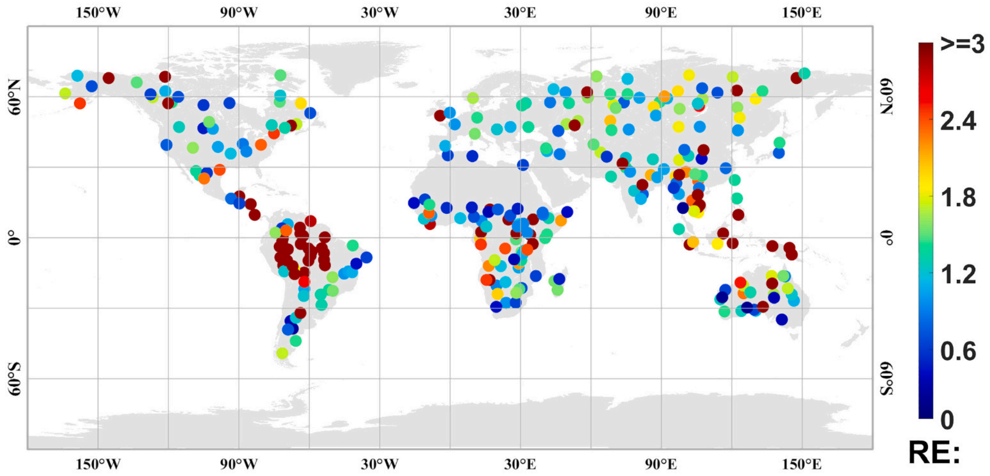

(b) Max-FPAR-VIIRS

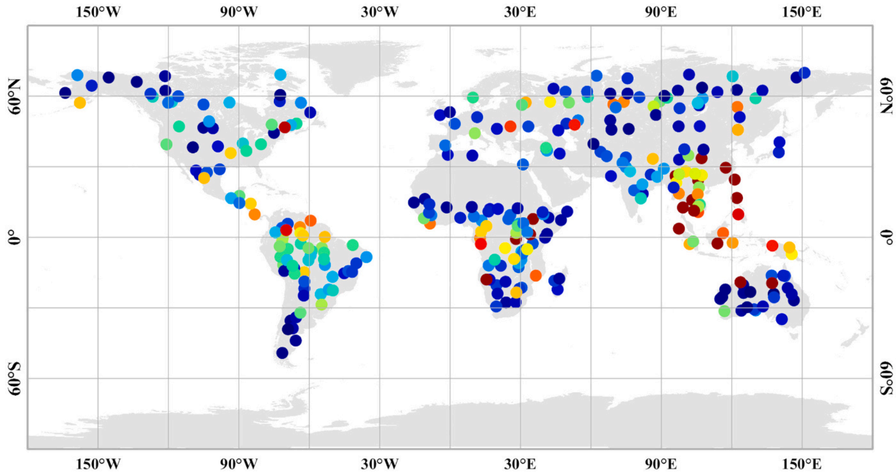

(c) PKA-MODIS

Fig. 10. The scatter plot of RE over BELMANIP 2.1 sites during 2021 for Max-FPAR-MODIS (a), Max-FPAR-VIIRS (b), and PKA-MODIS LAI (c).

the same trend; the multi-year value of the RE decreased from 2.37/2.35 to 2.25 (Fig. 8a) and the RI increased from 61.94%/59.62% to 66.88% (Fig. 8b). This is also consistent with the trend illustrated in Fig. 9, where the distributions of RE shift to the left from Max-FPAR-MODIS/Max-FPAR-VIIRS to PKA-MODIS LAI, while the distribution of RI shows a significant shift to the right.

3.4. *Interomparison over the BELMANIP 2.1 sites*

To further evaluate the performance of PKA in different biome types, scatter plots of RE extracted from the Max-FPAR-MODIS, Max-FPAR-VIIRS, and PKA-MODIS over BELMANIP2.1 sites during the year 2021 were shown in Fig. 10. This figure showed that the colour of PKA-MODIS tended to be blue (small RE) for most sites compared to the other two

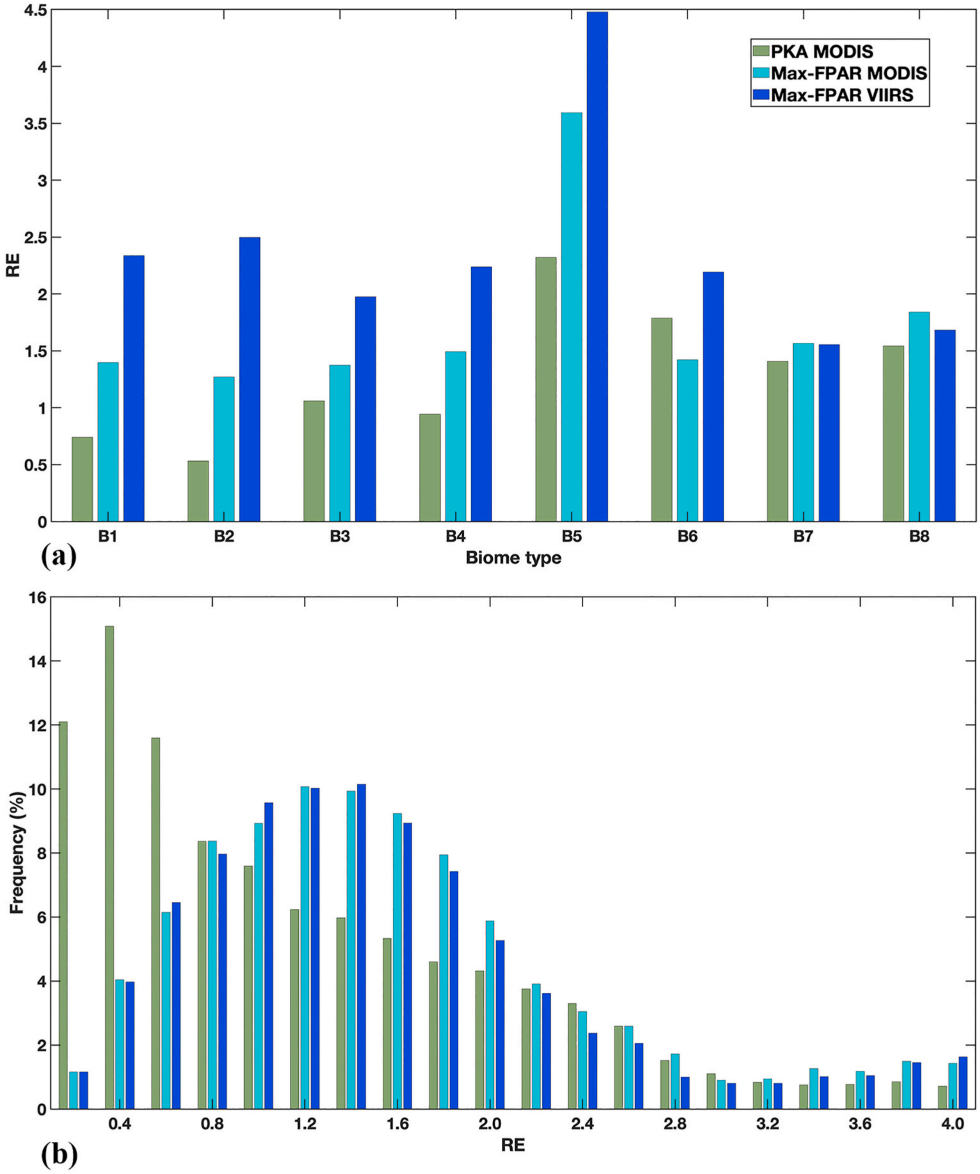

Fig. 11. Comparison of RE over BELMANIP 2.1 sites between MODIS-PKA, MODIS-Max-FPAR, and VIIRS-Max-FPAR LAIs for the year 2021. Panel (a) means that the comparison for different biome types and the panel (b) means the probability distribution of RE.

Max-FPAR retrievals, the RE of Max-FPAR-MODIS (1.85) and Max-FPAR-VIIRS (2.13) were all higher than PKA-MODIS (1.15). This point was consistent with the frequency illustrated in Fig. 11(b), where the distributions of RE turn to the left side from Max-FPAR-MODIS/Max-FPAR-VIIRS to PKA-MODIS LAI. From Fig. 11(a), the PKA shows the significant improvement for all biome types except B6. Specially, the PKA's RE of the non-forest biomes (B1-B4) were all much smaller than the Max-FPAR series, and the PKA's RE of needleaf forest biomes (B7-B8) also shows a slight decreasing trend. However, the comparison of broadleaf forest biomes is antagonistic, the RE of B5 (EBF) showed the significant decreasing trend after PKA's implementation but this trend was disappeared for the RE of B6 (DBF). Further results of the Fig. 12 show that the RE increases as the proportion of unqualified observations in the composite increases throughout all year. Conversely, the RE decreases when the proportion of qualified observations in the composite greater than or equal to 3 (take BRDF adjustment) increases over the whole year. This point not only proves the importance of qualified observations, but also the significance of introducing the prior information when qualified observations are not available indirectly.

4. Discussion

Our current results show that the PKA improves the performance for almost all biomes (Fig. 5, Fig. 6, and Fig. 11), especially for savannas and EBF, which can be attributed to the importance of time-series prior information. For those biomes that do not show significant seasonality at low latitudes, the PKA can make use of temporal prior information instead of the poor observations due to the cloud/aerosol to improve retrieval performance (section 3.1 and section 3.4). However, the PKA cannot overcome the uncertainty of LAI retrievals due to long-term snow cover, cloud cover, and large SZA/VZA, which may explain why the improvements of other biomes are not as significant as those of tropical biomes and the underestimation of both PKA and Mar-FPAR in winter. From the perspective of the ill-posed retrieval, the newly proposed PKA

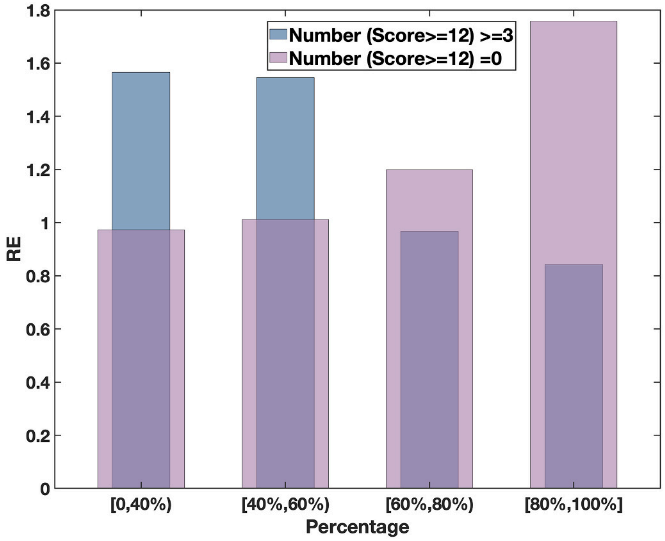

Fig. 12. RE as a function of the proportion of composites where the number of qualified observations (score $\geq$12) meets special requirements (number $\geq$3 or number = 0) for all composites for the year 2021 for PKA-MODIS LAI.

still fails to provide an accurate solution when there are insufficient observations. In addition, compared to Max-FPAR, the PKA significantly reduces the LAI fluctuations (section 3.2), as the proposed compositing algorithm can eliminate the directional effect of observations and the replacement of poor quality observations with prior information in some situations.

4.1. *Underlying causes of PKA's improvements*

MODIS Max-FPAR LAI has discontinuities in time scales, as the same pixel can have a large retrieval difference in neighboring composites, due to the daily retrieval process and the Max-FPAR compositing principle. During the daily retrieval process, the backup algorithm can be substituted if the main algorithm fails to find a solution. However, the backup algorithm is obtained by adapting the main RT-based algorithm and ignoring the sun-sensor geometry, resulting in a higher theoretical uncertainty than the main algorithm (Knyazikhin, 1999; Myneni and Park, 2015; Yan et al., 2016a). The backup algorithm is always triggered by two conditions: 1) poor sun-sensor geometries (i.e., large SZA or VZA); and 2) observed BRFs that are far from the retrieval space of the main algorithm (Fig. 13) due to poor observational conditions (e.g., clouds and aerosols). The effect of poor observational conditions on retrieval uncertainty is evident in Fig. 14, where LAI retrievals with higher scores (score $\geq$ 12) filtered by an observational condition scoring procedure have a higher probability of the main algorithm (higher RI, Fig. 14b) and less uncertainty (lower RD of LAI, Fig. 14a) in the retrieval process. For the above reasons, the uncertainties of the main and backup algorithms in the actual retrieval differ significantly. In addition, the Max-FPAR compositing algorithm selects the representative results based on the priority of the main algorithm and the Max-FPAR principle after the daily retrievals are completed. This can lead to several possible phenomena: 1) for adjacent composites, one group of observations are all poor and the algorithm paths are all backup, while the other group has high-quality observations and triggers the main algorithm, leading to large retrieval uncertainties at adjacent composites; 2) the Max-FPAR algorithm searches for one retrieval result within 8 days independently for adjacent composites, then there is a variable time difference (1 day or 15 days); 3) the Max-FPAR algorithm tends to consider atmospheric effects rather than sun-sensor geometry. For instance, if there are two daily retrievals with very close FPARs (the first group has a slightly higher FPAR but poor sun-sensor geometry, while the second group is the opposite), the Max-FPAR algorithm would select the first group, but the second retrieval is the most suitable retrieval for compositing. 4) the Max-FPAR algorithm would not take full advantage of the other suitable retrieval results. In summary, all these factors contribute to the uncertainty and instability of the LAI time series.

The PKA proposed in this study is improved in response to these problems. Firstly, the scoring procedure filters the observation conditions and observations with poor conditions are not included in the retrieval process unless the prior information is not available, which reduces the input uncertainty. Secondly, the weight of large SZA/VZA observations can also be reduced (Eq. (7)) due to high uncertainty. Thirdly, when the Max-FPAR principle uses the backup algorithm due to the lack of qualified observations in the time window, the weight of the prior knowledge will increase and then generate a set of observations with higher confidence for retrieval. The PKA moves from the pattern of initially using low quality observations and backup algorithms to the state where the prior knowledge and main algorithm are used for retrieval. Finally, when enough high-quality observations are available within this window, the BRDF adjustment model is used to make full use of the information from all qualifying observations, correct for BRDF directional effects, and upgrade the time prior information. All these points support that the PKA improves the retrieval accuracy and indirectly enhances the time-series stability.

4.2. *Limitation and future prospects*

In this study, the PKA is coupled with the MODIS operational LAI retrieval process and the BRDF-adjusted model, where some coefficients, steps, and limitations had to be clarified here.

Firstly, the coefficients in Table 1 were originally based on the SEVIRI sensor. We designed a series of single factor experiments aimed to explore the relationship between the retrieval uncertainty and the model parameters (i.e., coefficients c_1 and c_2 for the red and NIR bands, Eq. (3)). If we change one of the four parameters, the other three coefficients are fixed (Table 1) in the sensitivity experiments (Fig. S5). The R^2 would decrease with the increase of c_1 for the red band (when the c_1 red is 0.001, the R^2 is highest). As for c_2 red, the R^2 increases with the increase of c_2 red, and when the c_2 red $\geq$0.07, the R^2 no longer changes significantly with the increase of c_2 red. For the NIR band, the retrieval accuracy also does not vary with c_1 and c_2. In summary, we believe that the current parameter configuration is sufficient to accommodate the MODIS sensor.

Secondly, the observation with the smallest SZA and VZA is selected as the specific angle to generate BRF when making the BRDF adjustment. Similar to the coefficients c_1 and c_2, we designed the sensitivity experiments for VZA. As shown in Fig. S6, F in Eq. (2) as well as SZA are fixed, and K has changed accordingly when VZA and RAA are changed. The BRFs under different sun-sensor geometries are obtained and imported into the retrieval algorithm to obtain the LAI retrievals with uncertainty. Compared with the retrievals when the VZA is 0, we found that the larger the VZA, the greater the uncertainty. This is in agreement with the study of Pu et al., (2020).

Thirdly, the use of the 16-day prior knowledge window and the 8-day current window is suitable for production. Considering that the use of adaptive windows (e.g., number of observations greater than or equal to 3) might be suitable for retrieval, it seems that the adaptive windows might be a better choice. However, if we choose the adaptive windows that may allow high-frequency retrievals (perhaps daily) in some areas with qualified observations but very low retrieval frequency (perhaps monthly or longer) in some areas with long-term cloud/snow cover. The purpose of setting an inherent historical information window for 16d and an observational window for 8d is that we want the PKA to improve the retrieval accuracy without changing the input data and the core retrieval algorithm, and to allow the PKA to replace the current compositing algorithm in the future. In addition, from the product manufacturing perspective, using future data will introduce additional

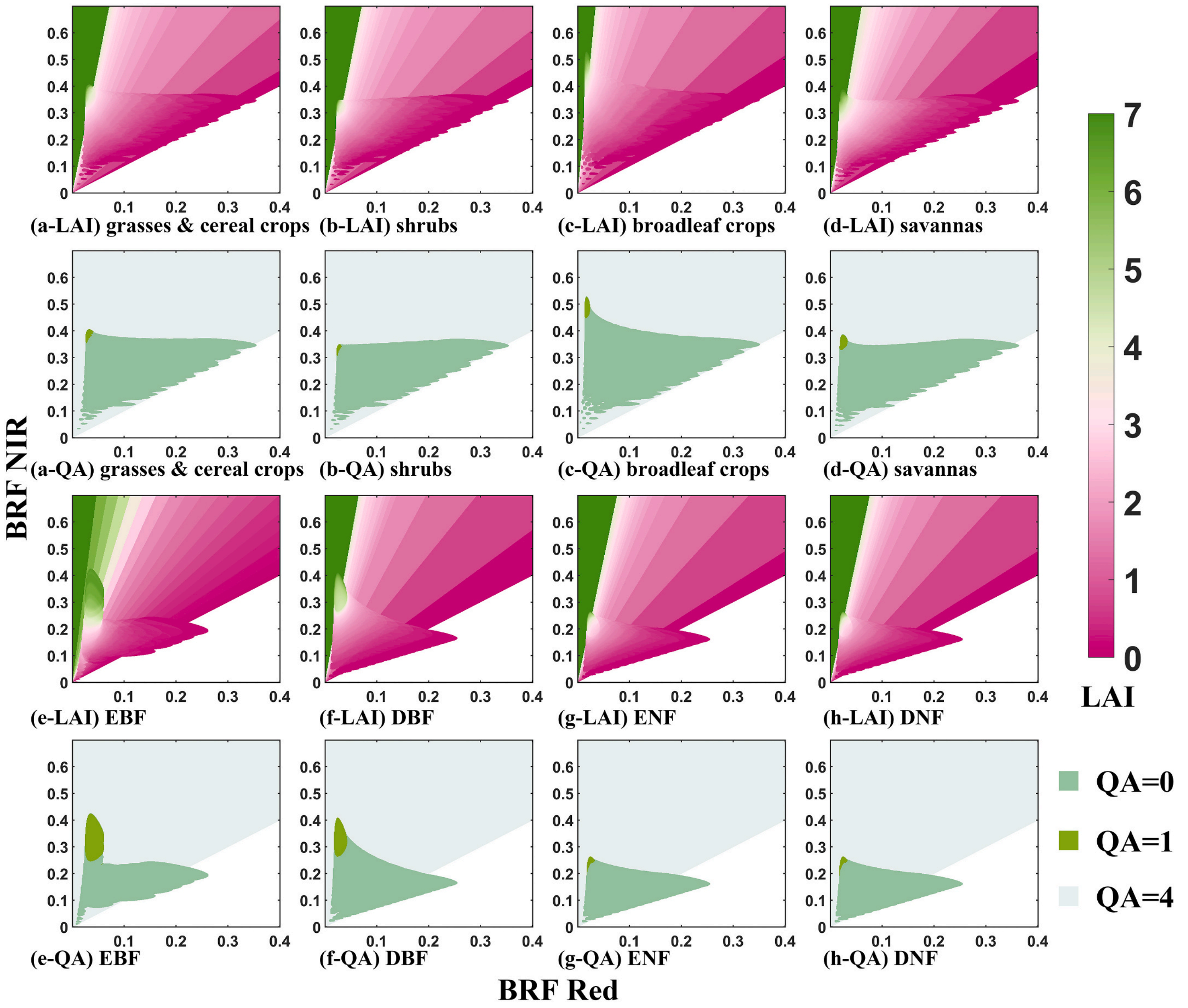

Fig. 13. Distribution of LAI values and associated algorithm paths derived from the main RT-based/backup empirical relationship-based algorithm in the red-NIR retrieval space. The SZA, VZA, and RAA are 30°, 0°, and 90°, respectively. Panels (a)-(h) are for eight biome types. The QA represents different algorithm paths (main algorithm without saturation (QA = 0), the main algorithm with saturation (QA = 1), the backup algorithm due to sun sensor geometry (QA = 3), and the backup algorithm due to other reasons (QA = 4)). (For interpretation of the references to colour in this figure legend, the reader is referred to the web version of this article.)

data and uncertainty. Thus, the combination of the 16-day prior knowledge window and the 8-day current window would allow PKA to improve product performance based on the original algorithm if certain conditions are met (the prior knowledge available or sufficient qualifying observations).

Fourthly, the uncertainty of BRDF-adjusted model needs to be discussed here. The LKD model is more applicable and has been adopted by many sensors due to its semi-empirical and convenient fitting properties (Schaaf et al., 2002). However, the BRDF-adjusted model also suffers from some shortcomings: 1) underestimation in the hotspot region, leading to high overall uncertainty at high latitudes (Li et al., 2022; Jiao et al., 2016). 2) semi-empirical properties will make the theoretical uncertainty of PKA higher than the original algorithm. Therefore, it is necessary to analyze the uncertainty that would result from the introduction of the BRDF-adjusted model before the compositing algorithm can be applied to large-scale applications in the future.

Fifthly, the RE-based results (Fig. 11 and Fig. 12) show that reconstruction errors are unavoidable for both Max-FAPR and PKA, which is attributed to the difference in retrieval accuracy between main (low RE) and backup (high RE) algorithms. In the process of reconstructing the LAI reference, only the retrievals of the main algorithm are used, while the original retrievals using the backup algorithm are replaced by the composites of the same dates in other years, whereas the Max-FPAR and PKA inevitably use the backup algorithm. This implied that the uncertainty of the LAI products based on the Max-FPAR and PKA methods would be potentially greater than the non-interpolated algorithm when the retrieval ratio of the main algorithm was low. However, the ground-based validations showed that the uncertainties of both Max-FPAR and PKA met the requirements of GCOS. The lower RE (RE ~ 0.4) of PKA compared to Max-FPAR (RE > 1) suggests that PKA uses a higher proportion of the main algorithm, resulting in a lower uncertainty. This also provides a clear direction for future algorithm improvement, i.e., to reduce the proportion of the backup algorithm and increase the proportion of the main algorithm as much as possible.

Finally, this work presented a preliminary validation of the new proposed algorithm. The PKA was only evaluated and validated at

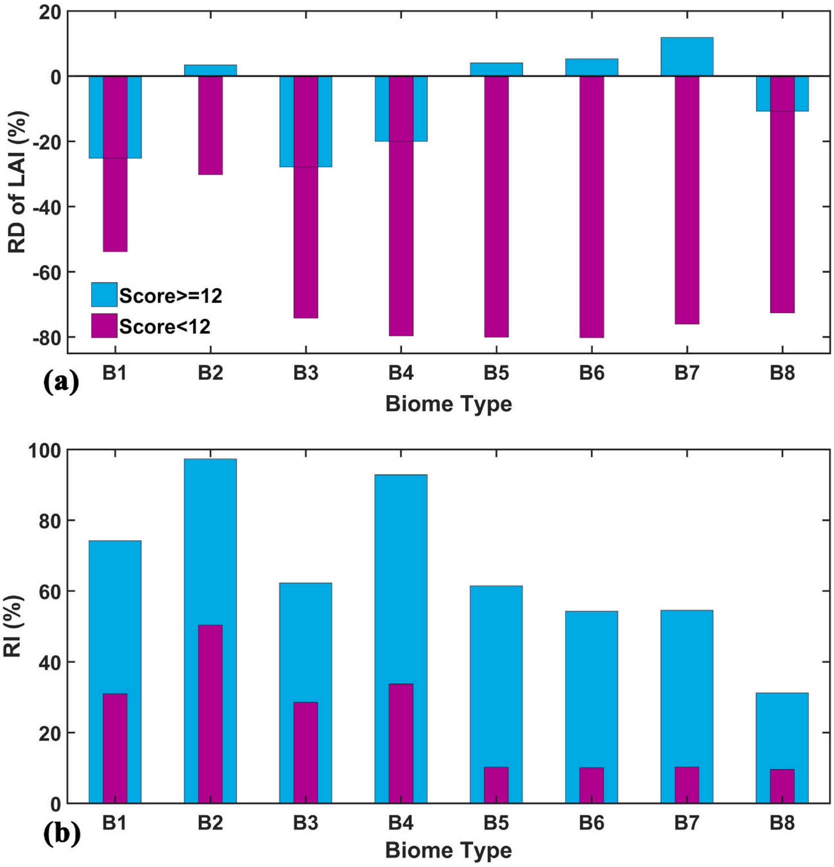

Fig. 14. Histograms of retrieval uncertainty for two observed groups of conditions (score <12) based on DIRECT 2.0 sites. (a) Relative difference (RD) of LAI and (b) retrieval index (RI). B1-B8 are eight biome types.

GBOV/NECC sites, selected forest-dominated region, and BELMANIP 2.1 sites for the year 2021. In the future, a more comprehensive evaluation and validation analysis of the PKA is needed (e.g., at the global scale and long-term period). In addition, this study focused only on LAI, and future studies could also be conducted on FPAR. In particular, it is worth investigating whether the Max-FPAR and PKA lead to an overestimation of FPAR. As this algorithm has the potential to be an operational algorithm, its efficiency compared to the previous Max-FPAR strategy should be investigated as a next step.

5. Conclusions

The MODIS LAI products employ different retrieval algorithms (algorithm path) depending on the quality of the observations, which is one of the main reasons for long-term instability of the LAI time series. The previous temporal compositing method based on the Max-FPAR principle was designed to reduce the variations in daily LAI retrievals. However, the Max-FPAR principle cannot take full advantage of all observations and the inconsistency of observation quality in adjacent composites could lead to deficiencies in retrieval accuracy and temporal continuity. Using a linear kernel-driven BRDF model, we proposed a prior knowledge time-series compositing algorithm (PKA) without changing the original daily retrieval algorithm. We validated and evaluated the PKA LAI at site and regional scales, respectively. Our results confirmed that the PKA provides significant improvements over the Max-FPAR strategy. The R^2 was improved from 0.69/0.23 (GBOV/NECC sites) to 0.76/0.41 and the RMSE were reduced from 1.01/1.27 to 0.84/1.25 in a site-scale comparison. In addition, most of the 16 sites studied (14 GBOV sites, Honghe site, and Hailun site) showed better time-series smoothness (indicated by three proposed temporal uncertainty metrics, TSS: time series stability, TSA: time series anomalies, and RE: reconstruction error metric that means the proximity to the main algorithm) for the new compositing strategy. The improvement also occurred in the Amazon Forest region and the BELMANIP 2.1 sites, which can be attributed to the fact that the PKA performed closer to the main RT-based retrievals compared to Max-FPAR. In conclusion, the newly proposed PKA can improve the LAI retrieval accuracy and its temporal stability, which gives it the potential to be selected as the official composting algorithm of the next MODIS or MODIS-like LAI Collections. This temporal compositing approach, incorporating time-series information from the BRDF perspective, also provides a new way to produce the time-series of other earth observation parameters.

CRediT authorship contribution statement

Jiabin Pu: Methodology, Conceptualization, Software, Formal analysis, Writing – original draft. **Kai Yan:** Writing – review & editing, Funding acquisition, Investigation. **Si Gao:** Writing – review & editing, Formal analysis. **Yiman Zhang:** Writing – review & editing, Software. **Taejin Park:** Investigation. **Xian Sun:** Investigation. **Marie Weiss:** Supervision, Conceptualization, Methodology. **Yuri Knyazikhin:** Supervision, Resources. **Ranga B. Myneni:** Conceptualization, Resources, Supervision.

Declaration of Competing Interest

The authors declare that they have no known competing financial interests or personal relationships that could have appeared to influence the work reported in this paper.

Data availability

Data will be made available on request.

Acknowledgments

This work was supported in part by the National Natural Science Foundation of China under Grant 42271356 and 41901298 and in part by the Fundamental Research Funds for the Central Universities under Grant 265QZ2022001.

Appendix A. Supplementary data

Supplementary data to this article can be found online at https://doi.org/10.1016/j.rse.2023.113493.

References

1 Asaadi, A., Arora, V.K., Melton, J.R., Bartlett, P., 2018. An improved parameterization of leaf area index (LAI) seasonality in the Canadian land surface scheme (CLASS) and Canadian terrestrial ecosystem model (CTEM) modelling framework. Biogeosciences 15 (22), 6885–6907.

2 Azzali, S., Menenti, M., 1999. Mapping isogrowth zones on continental scale using temporal fourier analysis of AVHRR-NDVI data. Int. J. Appl. Earth Obs. Geoinf. 1 (1), 9–20.

3 Bacour, C., Bréon, F.M., Maignan, F., 2006. Normalization of the directional effects in NOAA–AVHRR reflectance measurements for an improved monitoring of vegetation cycles. Remote Sens. Environ. 102 (3–4), 402–413.

4 Bai, G., Dash, J., Brown, L., Meier, C., Lerebourg, C., Ronco, E., Gobron, N., 2019. GBOV (ground-based observation for validation): a copernicus service for validation of vegetation land products. In: IGARSS 2019-2019 IEEE International Geoscience and Remote Sensing Symposium (pp. 4592-4594). IEEE.

5 Baret, F., Morissette, J.T., Fernandes, R.A., Champeaux, J.L., Myneni, R.B., Chen, J., Nickeson, J.E., 2006. Evaluation of the representativeness of networks of sites for the global validation and intercomparison of land biophysical products: proposition of the CEOS-BELMANIP. IEEE Trans. Geosci. Remote Sens. 44 (7), 1794–1803.

6 Baret, F., Weiss, M., Lacaze, R., Camacho, F., Makhmara, H., Pacholcyzk, P., Smets, B., 2013. GEOV1: LAI and FAPAR essential climate variables and FCOVER global time series capitalizing over existing products. Part1: principles of development and production. Remote Sens. Environ. 137, 299–309.

7 Bartholome, E., Belward, A.S., 2005. GLC2000: a new approach to global land cover mapping from earth observation data. Int. J. Remote Sens. 26 (9), 1959–1977.

8 Beck, P.S., Atzberger, C., Høgda, K.A., Johansen, B., Skidmore, A.K., 2006. Improved monitoring of vegetation dynamics at very high latitudes: a new method using MODIS NDVI. Remote Sens. Environ. 100 (3), 321–334.

9 Bi, J., Knyazikhin, Y., Choi, S., Park, T., Barichivich, J., Ciais, P., Myneni, R.B., 2015. Sunlight mediated seasonality in canopy structure and photosynthetic activity of amazonian rainforests. Environ. Res. Lett. 10 (6), 064014.

10 Brown, L.A., Meier, C., Morris, H., Pastor-Guzman, J., Bai, G., Lerebourg, C., Dash, J., 2020. Evaluation of global leaf area index and fraction of absorbed photosynthetically active radiation products over North America using copernicus ground based observations for validation data. Remote Sens. Environ. 247, 111935.

11 Brown, L.A., Camacho, F., García-Santos, V., Origo, N., Fuster, B., Morris, H., Dash, J., 2021. Fiducial reference measurements for vegetation bio-geophysical variables: an end-to-end uncertainty evaluation framework. Remote Sens. 13 (16), 3194.

12 Bullock, E.L., Woodcock, C.E., Souza Jr., C., Olofsson, P., 2020. Satellite-based estimates reveal widespread forest degradation in the Amazon. Glob. Chang. Biol. 26 (5), 2956–2969.

13 Camacho, F., Cernicharo, J., Lacaze, R., Baret, F., Weiss, M., 2013. GEOV1: LAI, FAPAR essential climate variables and FCOVER global time series capitalizing over existing products. Part 2: validation and intercomparison with reference products. Remote Sens. Environ. 137, 310–329.

14 Chakroun, H., Mouillot, F., Nasr, Z., Nouri, M., Ennajah, A., Ourcival, J.M., 2014. Performance of LAI-MODIS and the influence on drought simulation in a Mediterranean forest. Ecohydrology 7 (3), 1014–1028.

15 Chen, C., Knyazikhin, Y., Park, T., Yan, K., Lyapustin, A., Wang, Y., Myneni, R.B., 2017. Prototyping of LAI and FPAR retrievals from MODIS multi-angle implementation of atmospheric correction (MAIAC) data. Remote Sens. 9 (4), 370.

16 Chen, C., Park, T., Wang, X., Piao, S., Xu, B., Chaturvedi, R.K., Myneni, R.B., 2019. China and India lead in greening of the world through land-use management. Nat. Sustain. 2 (2), 122–129.

17 Chen, C., Riley, W.J., Prentice, I.C., Keenan, T.F., 2022. CO2 fertilization of terrestrial photosynthesis inferred from site to global scales. Proc. Natl. Acad. Sci. 119 (10), e2115627119.

18 Chen, J.M., Black, T.A., 1992. Defining leaf area index for non-flat leaves. Plant Cell Environ. 15 (4), 421–429.

19 Chen, L., Dirmeyer, P.A., 2016. Adapting observationally based metrics of biogeophysical feedbacks from land cover/land use change to climate modeling. Environ. Res. Lett. 11 (3), 034002.

20 Cihlar, J., Manak, D., D'Iorio, M., 1994. Evaluation of compositing algorithms for AVHRR data over land. IEEE Trans. Geosci. Remote Sens. 32 (2), 427–437.

21 Dhorde, A.G., Patel, N.R., 2016. Spatio-temporal variation in terminal drought over western India using dryness index derived from long-term MODIS data. Ecol. Inform. 32, 28–38.

22 Fang, H., Baret, F., Plummer, S., Schaepman-Strub, G., 2019. An overview of global leaf area index (LAI): methods, products, validation, and applications. Rev. Geophys. 57 (3), 739–799.

23 Fang, H., Jiang, C., Li, W., Wei, S., Baret, F., Chen, J.M., Zhu, Z., 2013. Characterization and intercomparison of global moderate resolution leaf area index (LAI) products: analysis of climatologies and theoretical uncertainties. J. Geophys. Res. Biogeosci. 118 (2), 529–548.

24 Fang, H., Wei, S., Liang, S., 2012. Validation of MODIS and CYCLOPES LAI products using global field measurement data. Remote Sens. Environ. 119, 43–54.

25 Fang, H., Zhang, Y., Wei, S., Li, W., Ye, Y., Sun, T., Liu, W., 2019. Validation of global moderate resolution leaf area index (LAI) products over croplands in northeastern China. Remote Sens. Environ. 233, 111377.

26 Fang, H., Li, W., Wei, S., Jiang, C., 2014. Seasonal variation of leaf area index (LAI) over paddy rice fields in NE China: intercomparison of destructive sampling, LAI-2200, digital hemispherical photography (DHP), and AccuPAR methods. Agric. For. Meteorol. 198, 126–141.

27 Fang, H., Ye, Y., Liu, W., Wei, S., Ma, L., 2018. Continuous estimation of canopy leaf area index (LAI) and clumping index over broadleaf crop fields: an investigation of the PASTIS-57 instrument and smartphone applications. Agric. For. Meteorol. 253, 48–61.

28 Fang, H., 2021. Vegetation structural field measurement data for northeastern China crops (NECC). PANGAEA, Bremerhaven, Germany.

29 Fuster, B., Sánchez-Zapero, J., Camacho, F., García-Santos, V., Verger, A., Lacaze, R., Smets, B., 2020. Quality assessment of PROBA-V LAI, fAPAR and fCOVER collection 300 m products of copernicus global land service. Remote Sens. 12 (6), 1017.

30 Garrigues, S., Lacaze, R., Baret, F.J.T.M., Morisette, J.T., Weiss, M., Nickeson, J.E., Yang, W., 2008. Validation and intercomparison of global leaf area index products derived from remote sensing data. Journal of geophysical researchBiogeosciences 113 (G2).

31 Gcos, G., 2011. Systematic observation requirements for satellite-based products for climate. 2011 update supplemetnatl details to the satellite 39 based component og the implementation plan for the global observing system for climate in support of the UNFCCC (2010 update). Technical Report.

32 Geiger, B., Carrer, D., Franchisteguy, L., Roujean, J.L., Meurey, C., 2008. Land surface albedo derived on a daily basis from meteosat second generation observations. IEEE Trans. Geosci. Remote Sens. 46 (11), 3841–3856.

33 Hagolle, O., Lobo, A., Maisongrande, P., Cabot, F., Duchemin, B., De Pereyra, A., 2005. Quality assessment and improvement of temporally composited products of remotely sensed imagery by combination of VEGETATION 1 and 2 images. Remote Sens. Environ. 94 (2), 172–186.

34 Hilker, T., Lyapustin, A.I., Hall, F.G., Myneni, R., Knyazikhin, Y., Wang, Y., Sellers, P. J., 2015. On the measurability of change in Amazon vegetation from MODIS. Remote Sens. Environ. 166, 233–242.

35 Hill, M.J., Senarath, U., Lee, A., Zeppel, M., Nightingale, J.M., Williams, R.D.J., McVicar, T.R., 2006. Assessment of the MODIS LAI product for australian ecosystems. Remote Sens. Environ. 101 (4), 495–518.

36 Huang, D., Knyazikhin, Y., Wang, W., Deering, D.W., Stenberg, P., Shabanov, N., Myneni, R.B., 2008. Stochastic transport theory for investigating the three-dimensional canopy structure from space measurements. Remote Sens. Environ. 112 (1), 35–50.

37 Huntzinger, D.N., Schwalm, C., Michalak, A.M., Schaefer, K., King, A.W., Wei, Y., Zhu, Q., 2013. The north american carbon program multi-scale synthesis and terrestrial model intercomparison project–part 1: overview and experimental design. Geosci. Model Dev. 6 (6), 2121–2133.

38 Holben, B.N., 1986. Characteristics of maximum-value composite images from temporal AVHRR data. Int. J. Remote Sens. 7 (11), 1417–1434.

39 Jiao, Z., Schaaf, C.B., Dong, Y., Román, M., Hill, M.J., Chen, J.M., Strahler, A., 2016. A method for improving hotspot directional signatures in BRDF models used for MODIS. Remote Sens. Environ. 186, 135–151.

40 Jönsson, P., Eklundh, L., 2004. TIMESAT—a program for analyzing time-series of satellite sensor data. Comput. Geosci. 30 (8), 833–845.

41 Knyazikhin, Y., 1999. MODIS leaf area index (LAI) and fraction of photosynthetically active radiation absorbed by vegetation (FPAR) product (MOD 15) algorithm theoretical basis document. https://modis.gsfc.nasa.gov/data/atbd/atbd_mod15.pdf.

42 Knyazikhin, Y., Martonchik, J.V., Myneni, R.B., Diner, D.J., Running, S.W., 1998. Synergistic algorithm for estimating vegetation canopy leaf area index and fraction of absorbed photosynthetically active radiation from MODIS and MISR data. J. Geophys. Res. Atmos. 103 (D24), 32257–32275.

43 Lafont, S., Zhao, Y., Calvet, J.C., Peylin, P., Ciais, P., Maignan, F., Weiss, M., 2012. Modelling LAI, surface water and carbon fluxes at high-resolution over France: comparison of ISBA-A-gs and ORCHIDEE. Biogeosciences 9 (1), 439–456.

44 León-Tavares, J., Roujean, J.L., Smets, B., Wolters, E., Toté, C., Swinnen, E., 2021. Correction of directional effects in VEGETATION NDVI time-series. Remote Sens. 13 (6), 1130.

45 Li, H., Yan, K., Gao, S., Song, W., Mu, X., 2022. Revisiting the performance of the kernel-driven BRDF model using filtered high-quality POLDER observations. Forests 13 (3), 435.

46 Li, X., Huang, H., Shabanov, N.V., Chen, L., Yan, K., Shi, J., 2020. Extending the stochastic radiative transfer theory to simulate BRF over forests with heterogeneous distribution of damaged foliage inside of tree crowns. Remote Sens. Environ. 250, 112040.

47 Li, X., Du, H., Mao, F., Zhou, G., Han, N., Xu, X., Zhang, M., 2019. Assimilating spatiotemporal MODIS LAI data with a particle filter algorithm for improving carbon cycle simulations for bamboo forest ecosystems. Sci. Total Environ. 694, 133803.
48 Liu, Y., Xiao, J., Ju, W., Zhu, G., Wu, X., Fan, W., Zhou, Y., 2018. Satellite-derived LAI products exhibit large discrepancies and can lead to substantial uncertainty in simulated carbon and water fluxes. Remote Sens. Environ. 206, 174–188.
49 Mao, J., Shi, X., Thornton, P.E., Hoffman, F.M., Zhu, Z., Myneni, R.B., 2013. Global latitudinal-asymmetric vegetation growth trends and their driving mechanisms: 1982–2009. Remote Sens. 5 (3), 1484–1497.
50 Mariano, D.A., dos Santos, C.A., Wardlow, B.D., Anderson, M.C., Schiltmeyer, A.V., Tadesse, T., Svoboda, M.D., 2018. Use of remote sensing indicators to assess effects of drought and human-induced land degradation on ecosystem health in northeastern Brazil. Remote Sens. Environ. 213, 129–143.
51 Myneni, R., Park, Y.K.T., 2015. MODIS collection 6 (C6) LAI/FPAR product user's guide.
52 Myneni, R.B., Hoffman, S., Knyazikhin, Y., Privette, J.L., Glassy, J., Tian, Y., Running, S.W., 2002. Global products of vegetation leaf area and fraction absorbed PAR from year one of MODIS data. Remote Sens. Environ. 83 (1–2), 214–231.
53 Park, T., Yan, K., Chen, C., Xu, B., Knyazikhin, Y., Myneni, R., 2017. VIIRS Leaf Area index (LAI)and Fraction of Photosynthetically Active Radiation Absorbed by Vegetation (FPAR) Product Algorithm Theoretical Basis Document (ATBD). NASA Technical Report.
54 Pu, J., Yan, K., Zhou, G., Lei, Y., Zhu, Y., Guo, D., Myneni, R.B., 2020. Evaluation of the MODIS LAI/FPAR algorithm based on 3D-RTM simulations: a case study of grassland. Remote Sens. 12 (20), 3391.
55 Ql, J., Kerr, Y., 1997. On current compositing algorithms. Remote Sens. Rev. 15 (1–4), 235–256.
56 Qin, Y., Xiao, X., Wigneron, J.P., Ciais, P., Brandt, M., Fan, L., Moore, B., 2021. Carbon loss from forest degradation exceeds that from deforestation in the brazilian Amazon. Nat. Clim. Chang. 11 (5), 442–448.
57 Quaife, T., Lewis, P., 2010. Temporal constraints on linear BRDF model parameters. IEEE Trans. Geosci. Remote Sens. 48 (5), 2445–2450.
58 Rappaport, D.I., Morton, D.C., Longo, M., Keller, M., Dubayah, R., Santos, M.N., 2018. Quantifying long-term changes in carbon stocks and forest structure from Amazon forest degradation. Environ. Res. Lett. 13 (6), 065013.
59 Roujean, J.L., 2000. A parametric hot spot model for optical remote sensing applications. Remote Sens. Environ. 71 (2), 197–206.
60 Roujean, J.L., 2018. Inversion of lumped parameters using BRDF kernels. Comprehens. Remote Sens. 23–24.
61 Roujean, J.L., Leon-Tavares, J., Smets, B., Claes, P., De Coca, F.C., Sanchez-Zapero, J., 2018. Surface albedo and toc-r 300 m products from PROBA-V instrument in the framework of copernicus global land service. Remote Sens. Environ. 215, 57–73.
62 Roujean, J.L., Leroy, M., Deschamps, P.Y., 1992. A bidirectional reflectance model of the Earth's surface for the correction of remote sensing data. J. Geophys. Res. Atmos. 97 (D18), 20455–20468.
63 Schaaf, C.B., Gao, F., Strahler, A.H., Lucht, W., Li, X., Tsang, T., Roy, D., 2002. First operational BRDF, albedo nadir reflectance products from MODIS. Remote Sens. Environ. 83 (1–2), 135–148.
64 Savitzky, A., Golay, M.J., 1964. Smoothing and differentiation of data by simplified least squares procedures. Anal. Chem. 36 (8), 1627–1639.
65 Sellers, P.J., Dickinson, R.E., Randall, D.A., Betts, A.K., Hall, F.G., Berry, J.A., Henderson-Sellers, A., 1997. Modeling the exchanges of energy, water, and carbon between continents and the atmosphere. Science 275 (5299), 502–509.
66 Serbin, S.P., Ahl, D.E., Gower, S.T., 2013. Spatial and temporal validation of the MODIS LAI and FPAR products across a boreal forest wildfire chronosequence. Remote Sens. Environ. 133, 71–84.
67 Sulla-Menashe, D., Friedl, M.A., 2018. In: User Guide to Collection 6 MODIS Land Cover (MCD12Q1 and MCD12C1) Product, 1. USGS, Reston, VA, USA, p. 18.
68 Tang, X., Wang, Z., Xie, J., Liu, D., Desai, A.R., Jia, M., Liu, B., 2013. Monitoring the seasonal and interannual variation of the carbon sequestration in a temperate deciduous forest with MODIS time series data. For. Ecol. Manag. 306, 150–160.
69 Vancutsem, C., Pekel, J.F., Bogaert, P., Defourny, P., 2007. Mean compositing, an alternative strategy for producing temporal syntheses. Concepts and performance assessment for SPOT VEGETATION time series. Int. J. Remote Sens. 28 (22), 5123–5141.
70 Verger, A., Baret, F., Weiss, M., Kandasamy, S., Vermote, E., 2013. The CACAO method for smoothing, gap filling, and characterizing seasonal anomalies in satellite time series. IEEE Trans. Geosci. Remote Sens. 51 (4), 1963–1972.
71 Vermote, E.F., Kotchenova, S.Y., Ray, J.P., 2011. MODIS surface reflectance user's guide. In: MODIS Land Surface Reflectance Science Computing Facility version 1.
72 Vermote, E.F., Vermeulen, A., 1999. Atmospheric correction algorithm: spectral reflectances (MOD09). ATBD Vers. 4, 1–107.
73 Viovy, N., Arino, O., Belward, A.S., 1992. The best index slope extraction (BISE): a method for reducing noise in NDVI time-series. Int. J. Remote Sens. 13 (8), 1585–1590.
74 Wang, C., Li, J., Liu, Q., Zhong, B., Wu, S., Xia, C., 2017. Analysis of differences in phenology extracted from the enhanced vegetation index and the leaf area index. Sensors 17 (9), 1982.
75 Wang, Y., Li, X., Nashed, Z., Zhao, F., Yang, H., Guan, Y., Zhang, H., 2007. Regularized kernel-based BRDF model inversion method for ill-posed land surface parameter retrieval. Remote Sens. Environ. 111 (1), 36–50.
76 Wanner, W., Li, X., Strahler, A.H., 1995. On the derivation of kernels for kernel-driven models of bidirectional reflectance. J. Geophys. Res. Atmos. 100 (D10), 21077–21089.
77 Weiss, M., Baret, F., Block, T., Koetz, B., Burini, A., Scholze, B., Sanchez-Azofeifa, A., 2014. On line validation exercise (OLIVE): a web based service for the validation of medium resolution land products.Application to FAPAR products. Remote Sens. 6 (5), 4190–4216.
78 Weiss, M., Baret, F., Garrigues, S., Lacaze, R., 2007. LAI and fAPAR CYCLOPES global products derived from VEGETATION. Part 2: validation and comparison with MODIS collection 4 products. Remote Sens. Environ. 110 (3), 317–331.
79 Xiao, Z., Liang, S., Wang, J., Chen, P., Yin, X., Zhang, L., Song, J., 2013. Use of general regression neural networks for generating the GLASS leaf area index product from time-series MODIS surface reflectance. IEEE Trans. Geosci. Remote Sens. 52 (1), 209–223.
80 Xu, B., Li, J., Park, T., Liu, Q., Zeng, Y., Yin, G., Myneni, R.B., 2020. Improving leaf area index retrieval over heterogeneous surface mixed with water. Remote Sens. Environ. 240, 111700.
81 Xu, B., Park, T., Yan, K., Chen, C., Zeng, Y., Song, W., Myneni, R.B., 2018. Analysis of global LAI/FPAR products from VIIRS and MODIS sensors for spatio-temporal consistency and uncertainty from 2012–2016. Forests 9 (2), 73.
82 Yan, K., Park, T., Chen, C., Xu, B., Song, W., Yang, B., Myneni, R.B., 2018. Generating global products of LAI and FPAR from SNPP-VIIRS data: theoretical background and implementation. IEEE Trans. Geosci. Remote Sens. 56 (4), 2119–2137.
83 Yan, K., Park, T., Yan, G., Chen, C., Yang, B., Liu, Z., Myneni, R.B., 2016. Evaluation of MODIS LAI/FPAR product collection 6. Part 1: consistency and improvements. Remote Sens. 8 (5), 359.
84 Yan, K., Park, T., Yan, G., Liu, Z., Yang, B., Chen, C., Myneni, R.B., 2016. Evaluation of MODIS LAI/FPAR product collection 6. Part 2: validation and intercomparison. Remote Sens. 8 (6), 460.
85 Yan, K., Pu, J., Park, T., Xu, B., Zeng, Y., Yan, G., Myneni, R.B., 2021. Performance stability of the MODIS and VIIRS LAI algorithms inferred from analysis of long time series of products. Remote Sens. Environ. 260, 112438.
86 Yan, K., Zhang, Y., Tong, Y., Zeng, Y., Pu, J., Gao, S., Myneni, R.B., 2021. Modeling the radiation regime of a discontinuous canopy based on the stochastic radiative transport theory: modification, evaluation and validation. Remote Sens. Environ. 267, 112728.
87 Yan, K., Zou, D., Yan, G., Fang, H., Weiss, M., Rautiainen, M., Myneni, R.B., 2021. A bibliometric visualization review of the MODIS LAI/FPAR products from 1995 to 2020. J. Remote Sens. 2021, 7410921.
88 Yang, B., Knyazikhin, Y., Mõttus, M., Rautiainen, M., Stenberg, P., Yan, L., Myneni, R.B., 2017. Estimation of leaf area index and its sunlit portion from DSCOVR EPIC data: theoretical basis. Remote Sens. Environ. 198, 69–84.
89 Yang, W., Tan, B., Huang, D., Rautiainen, M., Shabanov, N.V., Wang, Y., Myneni, R. B., 2006. MODIS leaf area index products: from validation to algorithm improvement. IEEE Trans. Geosci. Remote Sens. 44 (7), 1885–1898.
90 Yin, G., Li, A., Jin, H., Zhao, W., Bian, J., Qu, Y., Xu, B., 2017. Derivation of temporally continuous LAI reference maps through combining the LAINet observation system with CACAO. Agric. For. Meteorol. 233, 209–221.
91 Zhang, Y., Song, C., Band, L.E., Sun, G., Li, J., 2017. Reanalysis of global terrestrial vegetation trends from MODIS products: Browning or greening? Remote Sens. Environ. 191, 145–155.
92 Zhou, J., Jia, L., Menenti, M., 2015. Reconstruction of global MODIS NDVI time series: performance of harmonic ANalysis of time series (HANTS). Remote Sens. Environ. 163, 217–228.
93 Zhou, J., Jia, L., Menenti, M., Gorte, B., 2016. On the performance of remote sensing time series reconstruction methods–A spatial comparison. Remote Sens. Environ. 187, 367–384.
94 Zhu, Z., Bi, J., Pan, Y., Ganguly, S., Anav, A., Xu, L., Myneni, R.B., 2013. Global data sets of vegetation leaf area index (LAI) 3g and fraction of photosynthetically active radiation (FPAR) 3g derived from global inventory modeling and mapping studies (GIMMS) normalized difference vegetation index (NDVI3g) for the period 1981 to 2011. Remote Sens. 5 (2), 927–948.
95 Zhu, Z., Piao, S., Myneni, R.B., Huang, M., Zeng, Z., Canadell, J.G., Zeng, N., 2016. Greening of the earth and its drivers. Nat. Clim. Chang. 6 (8), 791–795.
96 Zou, D., Yan, K., Pu, J., Gao, S., Li, W., Mu, X., Myneni, R.B., 2022. Revisit the performance of MODIS and VIIRS leaf area index products from the perspective of time-series stability. IEEE J. Sel. Top. Appl. Earth Obs. Remote Sens. 15, 8958–8973.